POLITECNICO DI TORINO

Master's Degree in Aerospace Engineering

Master's Degree Thesis

Spacecraft Micro-vibrations Analysis for Optical Communication Payloads

Supervisor
Prof. Dario G. Pastrone

Candidate
Samuele Raffa

Company Supervisor
German Aerospace Center (DLR)
Dr. Juraj Poliak

July 2020

Acknowledgements

As opposed to the novels told by author Lemony Snicket, what led me to write this thesis was A Series of Fortunate Events. There would not be the time nor the space to create a compilation of such Events, but I will try to remember all the people that made these possible.
First off, I would like to thank my supervisor Dr. Juraj Poliak for giving me the chance to work with him and his team during the development of the thesis. I would also like to thank my team leader Dr. Ramon Mata Calvo and all the colleagues I met at DLR-KN during these months. Among these, a special mention goes to the DLR-KN student colleagues: Cesar, Michael, Joana, Mareen and all the others, precious company and nice lunch (and sometimes dinner) mates.
I would like to thank all my friends and university colleagues, my second family, I met during my years at Politecnico, who kept supporting me even on a distance. Thanks to Francesco M. D., Claudio, Gaetano, Alessandro, Nicolò, Francesco G., Luca, Davide, Vito, Alessio P., Alessio L., Mariano, and Niki. I would also like to thank the Cubesat PoliTo Team and all of its members.
Last but not least, I would like to thank my family and my parents in particular, that always supported me on every decision I made on my life, even when they did not fully understand the reasons behind.

Summary

Current navigation systems on satellites base their measurements on synchronized signals from MEO constellations. The employment of Free-Space Optical (FSO) Communication for next-generation Kepler navigation constellation would bring several advantages, such as precise global synchronization, sub-millimetre ranging accuracy and high data-rate communication to allow a fast measurement exchange.
The core of this technology is represented by optical terminals, which are characterised by extremely narrow laser beams, with a divergence in the order of micro-radians. Hence, pointing requirement is critical for the payload performance. Extreme levels of required pointing accuracy bring new challenges in the design of the spacecraft, such as micro-vibrations management.
Micro-vibrations are low-level disturbances affecting the spacecraft during its nominal on-orbit operations, occurring in the 1 Hz - 1 kHz range. Engineering and research teams already demonstrated the possibility of solving this problem. Since the first experiments with ESA GEO optical data relay ARTEMIS spacecraft, progresses for a deeper knowledge about space micro-vibration environment have been made, which led to more and more reliable isolation systems and approaches. Nowadays, ESA EDRS spacecrafts represent a corner stone for FSO Communication systems.
In the past two decades, several solutions have been investigated and proposed to overcome the micro-vibrations criticality. Although, this spread of different concepts to address the same problem highlighted the necessity of identifying a baseline when starting a design of a new spacecraft with a payload susceptible to this low-magnitude mechanical disturbances. Lack of a common ground in terms to approach this problem led to the analysis in this thesis.
The thesis first provides an overview on statistical elements to investigate the stochastic nature of vibrations, along with reports from on-board measurements of spacecraft micro-vibrations. The so-called ESA model for micro-vibrations is analysed and reproduced through a simulation, that was used for an experiment between two optical terminals in the near-field range in order to investigate effects of the beam jitter at the receiving terminal.

Afterwards, several isolation systems already proposed in literature are discussed, encompassing both isolation and compensation systems, addressing platform-to-payload or disturbance-source-to-platform mechanical configurations.
In the final chapter, pointing requirements and optical terminal characteristics are entwined to assess the micro-vibration level the payload could withstand, to define a micro-vibration budget for the spacecraft.

Contents

List of Figures

List of Tables

Chapter 1

Introduction

Satellite communication systems have become part of daily life activities, providing media broadcast, network data and navigation services. Current Global Navigation Satellite Systems (GNSS) base their measurements on synchronized signals from MEO constellations. Lately, there have been proposals to substitute the current European Galileo GNSS with a more technological constellation. Among these, there is the Kepler GNSS constellation proposed by German Aerospace Center [1]. The employment of Free-Space Optical (FSO) Communication for next-generation Kepler navigation constellation would bring several advantages, such as precise global synchronization, sub-millimetre ranging accuracy and high data-rate communication to allow a fast measurement exchange. Employment of FSO communication payloads does not bring advantages only for data relay applications, but the technology can also be involved for interferometry and ranging systems to provide more accurate navigation systems, as it will be discussed in next sections.

1.1 Free-space Optical Communication

FSO communication has technological principles similar to optical fibre communication, with the main difference that the connection is performed through - indeed - free space beams, instead of light signals guided through silica fibres. Carriers for FSO Communication lie in the near infrared (NIR) range, with wavelengths between 700 nm and 2000 nm.
FSO Communication can count on several advantages with respect to classic RF systems [2]:

1. Increasing the carrier frequency, it is possible to increase the bandwidth of the channel. Ka-band frequency can go up to 40 GHz, while optical carriers

in the NIR range can easily be around 10^{16} Hz. Even if the maximum allowed bandwidth was 1% of the carrier frequency (usually it is higher, around 20% of the carrier frequency for RF systems), the theoretical bandwidth for the FSO channel would be around 100 THz.

2. The value of the beam divergence angle can be computed through the equation $\theta_{div} = 2.44(\lambda/D_R)$, with λ being the carrier wavelength and D_R the aperture diameter. Hence, the optical beam is characterised by a narrower θ_{div}, leading to an increased intensity of the signal at the receiver for the same power. In fig. 1.1 a graphical comparison between RF and optical beams is shown.

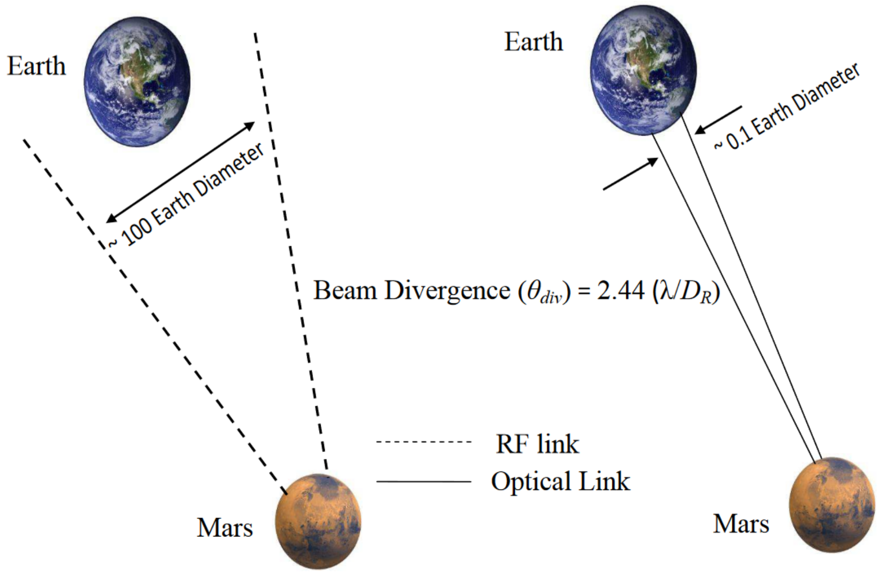

Figure 1.1: Comparison between RF and Optical beam divergence.[3].

This high directivity is related to the gain, and the advantage of the optical communication with respect to RF can be expressed as [4]:

$$\frac{\text{Gain}_{(opt)}}{\text{Gain}_{(RF)}} \sim \frac{4\pi/\theta^2_{div(opt)}}{4\pi/\theta^2_{div(RF)}} \tag{1.1}$$

With a narrower divergence angle for the optical carrier, the advantage in the gain appears clear.
This also leads to advantages in the system design: to achieve the same gain, a smaller antenna is required for the FSO system, resulting in a more compact, lighter and less power demanding product. It is shown in Table 1.1 a comparison for mass, power and size between two communication

systems: an optical one using 10 W, and a Ka-band one using 50 W, both for 2.5 Gbps communication. The systems are compared in different link configurations.

Link	Optical	RF
GEO-LEO		
Antenna Diameter	10.2 cm (1.0)	2.2 m (21.6)
Mass	65.3 kg (1.0)	152.8 kg (2.3)
Power	93.8 W (1.0)	213.9 W (2.3)
GEO-GEO		
Antenna Diameter	13.5 cm (1.0)	2.1 m (15.6)
Mass	86.4 kg (1.0)	145.8 kg (1.7)
Power	124.2 W (1.0)	204.2 W (1.6)
LEO-LEO		
Antenna Diameter	3.6 cm (1.0)	0.8 m (22.2)
Mass	23.0 kg (1.0)	55.6 kg (2.4)
Power	33.1 W (1.0)	77.8 W (2.3)

Table 1.1: Comparison between an optical and a RF communication system, with values in parentheses normalised to optical system parameters [5]

3. With respect to RF channels, at the time writing FSO communication is not required a spectrum licensing by regulatory authorities such as ITU, decreasing initial set up cost.

4. Due to the very narrow beam, interception of the signal is very difficult. Hence, FSO communication can provide a higher level as for security.

1.1.1 Heritage and Outlook

The first demonstration of a inter-satellite optical link was performed by ESA through its ARTEMIS Program [6]. The Program demonstrated optical inter-satellite LEO-GEO link between the ARTEMIS satellite (GEO) and SPOT-4 spacecraft (LEO), providing a data-relay service at 50 Mbps, with the optical link being unidirectional from SPOT-4 to ARTEMIS. The same experiment was performed between ARTEMIS and OICETS spacecrafts, this time demonstrating bidirectional link capabilities [7].

Promising results from such demonstrations brought to the investment and development of European Data Relay System (EDRS). This new program envisions a costellation of GEO satellites relaying data between lower orbit spacecrafts

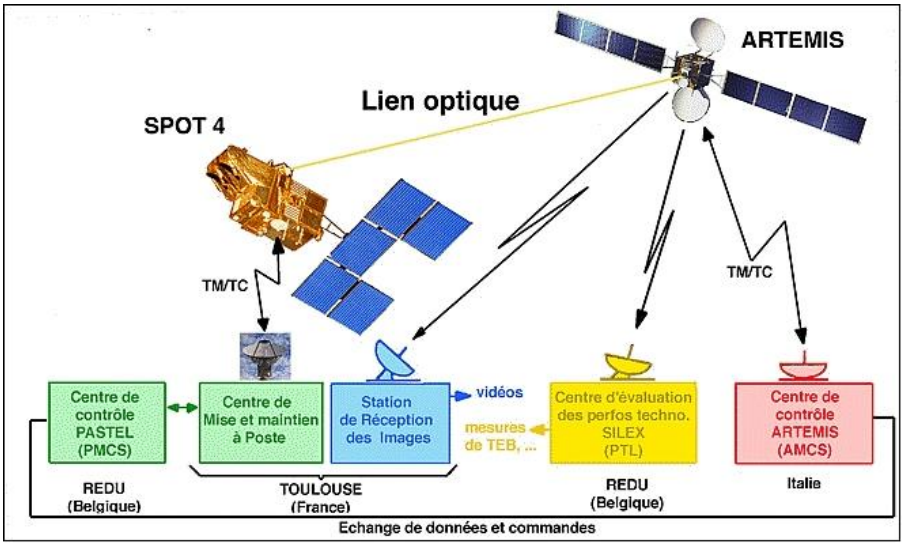

Figure 1.2: ARTEMIS - SPOT-4 communication architecture [image credit:CNES].

and ground stations. At the time writing, two EDRS payloads have been already launched, EDRS-A [8] and EDRS-C [9]. At the time writing, the system is mainly employed to relay data retrieved from LEO satellites through the optical link down to the ground stations using Ka-band antennas.

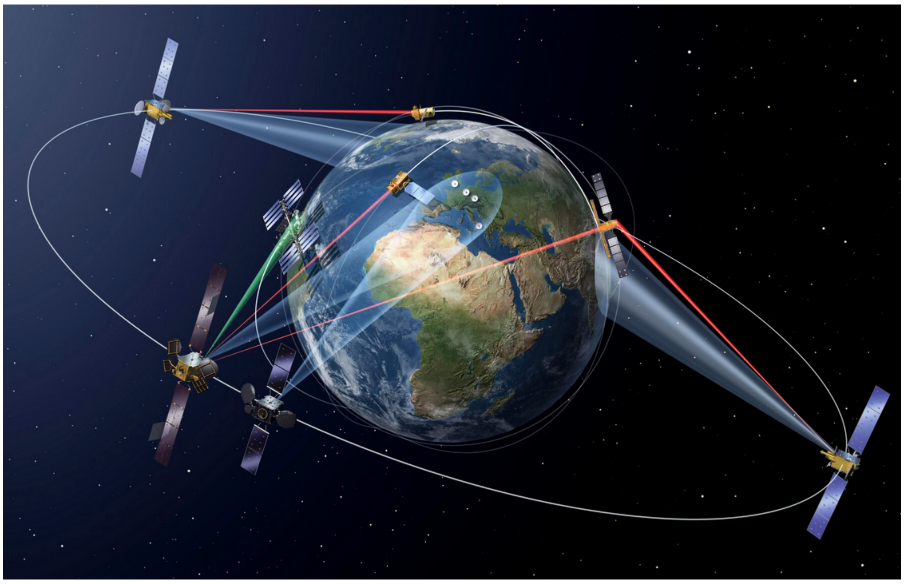

Figure 1.3: Visual representation of EDRS constellation and its communication architecture [image credit:ESA].

Although, FSO Communication can lead to critical improvements to other applications, such as ranging.
A good example for this is the GRACE mission, launched in 2002, and its follow-on GRACE-FO, deployed in 2018. GRACE (Gravity Recovery and Climate Experiment) missions are designed to investigate Earth's gravity field anomalies and climate change phenomena, employing a pair of twin satellites in flight formation. These anomalies are sensed measuring the distance between the two spacecrafts: in fact, in the presence of gravity anomalies, the relative distance would change. In GRACE this is performed through a microwave ranging system using a little Ka-band antenna. For its follow-on mission, GRACE-FO, to the microwave ranging system was added a Laser Ranging Interferometer (LRI) [10]. Despite resulting in only a marginal improvement for measurement accuracy, the Follow-On mission is an important demonstration for future ranging missions.

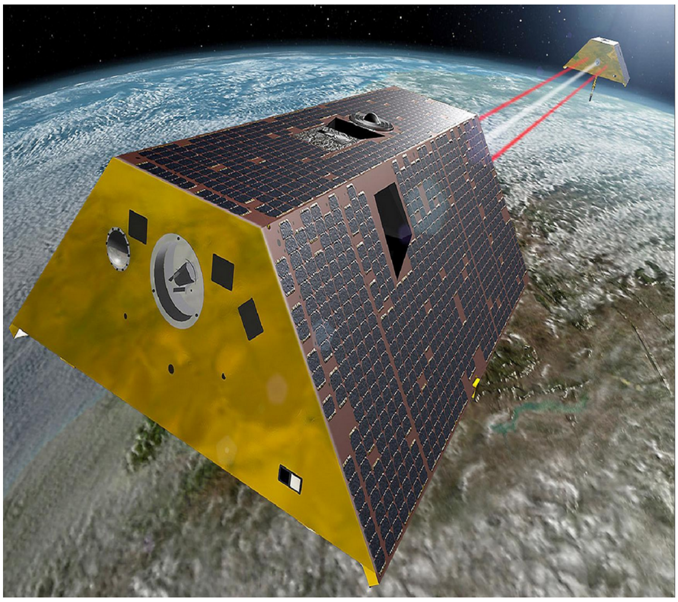

Figure 1.4: Render of GRACE-FO satellites in flight formation [image credit:AIRBUS DS].

1.2 Thesis Motivations

This thesis is developed in the context of a new project from German Aerospace Center (DLR), developed at the Institute for Communication and Navigation (KN), called Kepler. Kepler is a satellite constellation that inherits some of the characteristics from the current Galileo navigation constellation, but improving its performances through novel optical payloads [1]. Kepler will use an orbit

configuration similar to Galileo, with 24 MEO satellites (8 satellite for 3 orbital planes), with 4 additional LEO spacecrafts.
The two-way inter-satellite optical links will serve many functions:

- On the same MEO plane, adjacent spacecrafts will communicate to achieve global synchronization. In case of one spacecraft failure, the link can be performed with the next one.
- LEO-MEO links are employed to perform frequency transfer of the clock. In fact, LEO satellites mount iodine-stabilized lasers, that will act as the clocks of Kepler GNSS, whose frequency will be consistently updated to the MEO spacecrafts through the optical link.
- Through laser interferometry, it will be possible to achieve ranging (instead of pseudo-ranging as in common GNSS) between the constellation spacecrafts.
- All optical links also have communication capability, with a 50 Mbps data-rate.

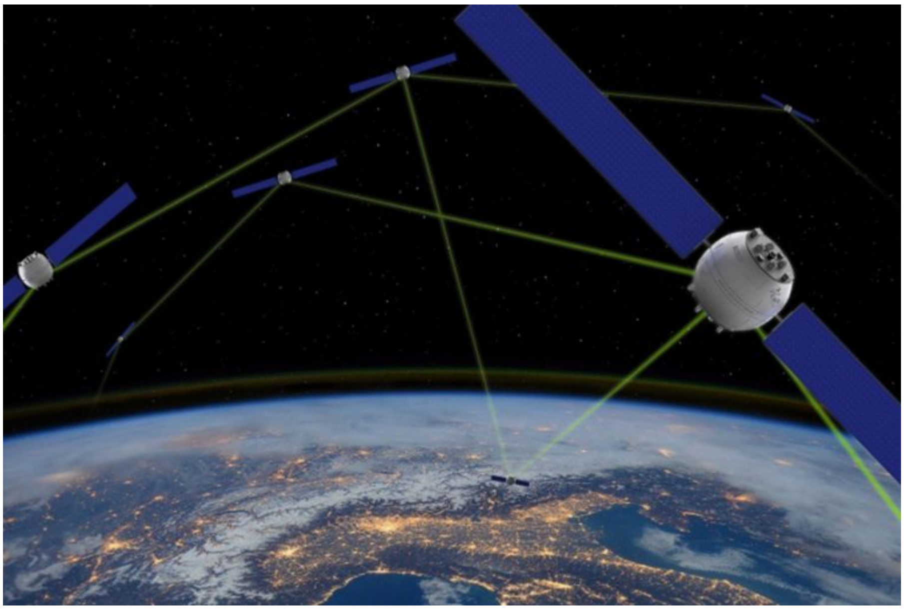

Figure 1.5: Render of Kepler Constellation, with optical links [image credit:DLR for Kepler constellation render, ESA/NASA for Earth render].

The higher stability of the Kepler clocks and its ranging capabilities would allow an enhanced accuracy in navigation systems, replacing the current Galileo GNSS constellation.

Although, multiple optical links will require a very stable platform to guarantee proper system performances.
To support the project, the thesis was developed to investigate micro-vibrations effects on pointing performance (jitter) for optical communication payloads. While there are guidelines provided by ESA [11, 12] and NASA [13], a common ground approach in the aeropsace industry is not present at the time writing . Hence, the aim of the thesis is to provide a survey on micro-vibrations, their effects and the way they are addressed in the literature. Furthermore, a simulation of the angular jitter was performed to investigate the misalignment effects between two laboratory terminals in DLR-KN.

1.3 Methodology and structure

The thesis is divided in three main chapters and the concluding chapter.
In Chapter 2, micro-vibrations and their stochastic nature are discussed. Through the chapter, statistical elements and the related terminology are presented, as they are used throughout the whole dissertation. Micro-vibrations sources are investigated with literature, in order to identify and address the critical sources in the following review of micro-vibration on-board measurements. This leads to the discussion of the ESA model and its simulation in the laboratory terminal, and finally preliminary results are discussed.
In Chapter 3, vibration damping and compensation approaches are investigated, discussing several systems and concepts retrieved from the literature, to provide a survey of the state of the art solutions that could be employed. This study was conducted focusing on most critical disturbance sources and payloads of interest for the research, therefore optical payloads and where possible specific FSO communication payloads.
In Chapter 4, most critical system-level analyses are discussed. This starts from requirements definition, studying relations between payload characteristics and micro-vibrations magnitude. Afterwards, spacecraft and source modelling are investigated, in order to assess a so-called micro-vibration budget. Then, using instruments discussed in Chapter 3, how to achieve disturbance minimisation is discussed, and finally how to perform the verification of the desired requirements is shown.
In Chapter 5, main conclusions drawn from previous chapters are discussed, thus leading to the end of the thesis.

Chapter 2

Spacecraft Micro-vibrations

Space-borne payloads precision has increased over the years (Fig.2.1), thus the platform stability requirements too. The need for more stable spacecraft platforms has driven improvement of Attitude Determination and Control System (ADCS) both in terms of actuators and sensors, in order to achieve and increasingly accurate pointing capability. Despite the enhanced ADCS performances, with sensors approaching angular resolution below 1 μrad, and FSO communications requiring a reduced angular jitter [14], new studies concerning lower vibration levels are required [15].
In this chapter, spacecraft micro-vibrations are introduced and their sources discussed and analysed. Statistical instruments are discussed too, in order to better understand disturbances behaviour. Moreover, effects of the induced pointing error on FSO communications are studied.

2.1 Micro-vibrations

Micro-vibrations are low-level disturbances affecting the spacecraft during its nominal on-orbit operations, occurring in the 1 Hz - 1 kHz range. This kind of disturbances does not represent a problem for most part of the spacecraft designs, but applications such as deep space observation, high resolution Earth observation and lately FSO communication have brought attention on the topic. The direct effect of these disturbances is an pointing jitter affecting the boresight. A good visualization of this effect is reported in fig 2.2.

These disturbances are critical due to their frequency range, where ADCS

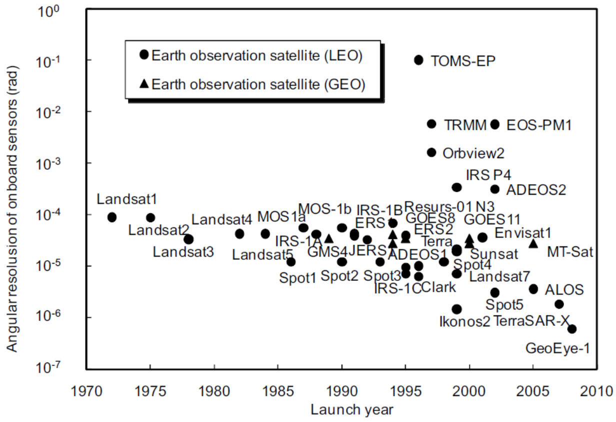

Figure 2.1: Trend of space imagers over the years [16]

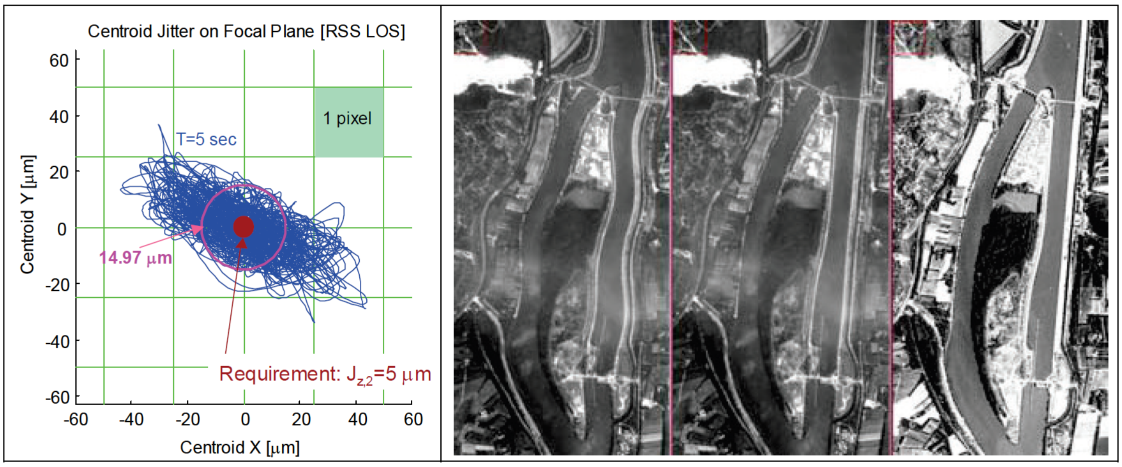

Figure 2.2: Jitter visualization. Left: visualization of boresight angular jitter on a focal plane. Right: effects of micro-vibrations on image quality [12]

sensors and actuators cannot counteract them. Being, as for definition, micro-vibrations oscillatory phenomena, statistical and signal processing methodology and instruments can come in handy, in order to assess the magnitude and the characteristics of such disturbances.

2.2 Statistical elements

In the following section, statistical functions and parameters will be introduced and used all along the discussion about pointing error performance. The following definitions are taken from [11].

2.2.1 Probability Density Function

Probability Distribution Function (not to be confused with Probability Density Function) is generally used to indicate the probability that a pointing error $e(k)$, depending on a set k of points, is less than a required pointing error e_r, hence respecting the inequality $e(k) < e_r$. In mathematical terms, it can be written as:

$$P_e = \text{Prob}[e(k) < e_r],$$
$$\text{with } P(-\infty) = 0 \text{ and } P(\infty) = 1.$$

But for pointing error analysis the usually addressed function is the Probability Density Function (PDF), defined, if the ensemble has a continuous range of values, as the derivative of the Probability Distribution Function:

$$p_e = \frac{dP_e}{de},$$
$$\text{with } \int_{-\infty}^{\infty} p(e)de = 1 \text{ and } p(e) = 1.$$

Statistical properties

Always considering the ensemble $e(k)$, a series of statistical properties, depending on the PDF, can be defined.

Mean value μ_e is defined as:

$$\mu_e = E[e(k)] = \int_{-\infty}^{\infty} ep(e)de.$$

Mean square value Ψ_e^2 is defined as:

$$\Psi_e^2 = E[e^2(k)] = \int_{-\infty}^{\infty} e^2 p(e)de.$$

Variance σ_e^2 is defined as:

$$\sigma_e^2 = \Psi_e^2 - \mu_e^2 = E[(e(k) - \mu_e)^2] = \int_{-\infty}^{\infty} (e - \mu_e)^2 p(e)de.$$

Root Mean Square (RMS) value is defined as:

$$RMS_e = \sqrt{\Psi_e^2}$$

Standard deviation σ_e corresponds to the RMS value in the only case mean value $\mu_e = 0$. In pointing error analysis, usually the RMS value is considered wih zero mean value, so that $\sigma_e = RMS_e$.

Gaussian and Rayleigh Distribution

As for micro-vibrations, pointing error along a single axis can be generally described by a Gaussian distribution. This will also help for the definition of the pointing requirements.
A Gaussian distribution is defined as:

$$p(e) = G(\mu_e, \sigma_e) = \frac{1}{\sigma_e\sqrt{2\pi}}^{-\frac{(e-\mu_e)^2}{2\sigma_e^2}} \tag{2.1}$$

Pointing error is usually defined along the two axes perpendicular to the pointing axis. Since along each in-plane axis the error is defined by a Gaussian distribution, the resulting bidimensional distribution would be a bivariate normal distribution. Although, in general the two Gaussian distributions are considered to be equal, as discussed in [11, 14, 16], hence the bidimensional distribution will be defined by a Rayleigh distribution:

$$p(e) = R(x, \sigma_R) = \frac{x}{\sigma_R^2} e^{-x^2/(2\sigma_R^2)}, \quad x \geq 0 \tag{2.2}$$

2.2.2 Power Spectral Density

In order to simplify the study of micro-vibrations effects on pointing error, some assumptions regarding their behaviour in the time domain are made.
The pointing error process $e_k(t)$ is assumed stationary; this means that statistical quantities (mean, variance, etc.) are equal for the time t. Most stationary random processes have a Gaussian PDF, so that they are defined simply by their mean and variance.
Moreover, a stationary process is said ergodic if the probability characteristics can be determined by time averages of arbitrary realizations k. This eases the pointing error analysis too, since statistical values can be determined simply using a single time series, instead of calculating an average value among several time series.

To describe the characteristics of the random stationary process in the frequency domain, an important statistical element is the Power Spectral Density (PSD).
In the frequency domain, the power of a signal is equivalent to the area underneath the even double sided PSD function S_{ee}:

$$\Phi_e^2 = R_{ee}(0) = \int_{-\infty}^{\infty} S_{ee}(f)df = \int_0^{\infty} 2S_{ee}(f)df = \int_0^{\infty} G_{ee}(f)df \tag{2.3}$$

The double-sided PSD function is noted as S_{ee}, while the single-sided one is noted as G_{ee}. The latter is more commonly found in micro-vibration analysis. Both present the frequency [Hz] in the x-axis and [unit^2/Hz] in the y-axis. In our case, the y-axis will show the [rad^2/Hz] value. PSD can be used as a meaningful characterisation of the disturbance magnitude related to each frequency.

2.3 Disturbance sources

In order to better understand the micro-vibration levels affecting a spacecraft, it is crucial to investigate all the possible disturbance sources involved. A logical decomposition, in accordance with [12] can allow us to classify the sources in two main categories: external and internal disturbances.

2.3.1 External disturbances

While space environment might seem mechanically quiet, it presents a challenging environment for spacecraft attitude control. Several disturbance sources can affect the spacecraft, namely: aerodynamic drag (for LEO missions); magnetic field; gravity field gradient; solar pressure and Earth albedo; impacts with micro-meteoroids and space debris (MMOD).
Exception made for MMOD impacts, that can be regarded as single-event disturbances, the rest of the external disturbances can be treated as slow transient or quasi-steady fluctuations. Thus, external disturbances are considered negligible in the context of microvibrations, as they are largely compensated by the ADCS.

2.3.2 Internal disturbances

Spacecraft subsystems can induce vibrations on the spacecraft itself, transferring these loads through the structure to the pointing-sensitive payload. This disturbance category is the most critical for our study, due to the multitude of subsystems, their mutual interaction and their broadband frequency micro-vibrations region.
Intuitively, the most critical subsystems are the ones where mechanical moving parts are involved, such as reaction wheels, cryo-coolers, thrusters, or solar arrays and antenna drives. Nevertheless, other events such as clank or structural sudden stress release could occur, introducing new vibrations. Main internal disturbances are listed in Table 2.1, along with their signal characteristics.

Source	Harmonic	Transient
Reaction wheels	X	
Control Momentum Gyros	X	
Gyroscopes	X	
Solar array drive mechanisms	(X)	X
Antenna pointing mechanisms		X
Mirror scan mechanisms		X
Cryogenic coolers	X	
Micro-thrusters, gas flow regulators		X
Latch valve		X
Heat pipe	X	
Relay, RF switch	X	
Sudden stress release	X	
Clank phenomena (e.g. electromagnetic force effects, MLI foil buckling)	X	

Table 2.1: Main internal disturbances [12]

Reaction Wheels

Reaction Wheel Assemblies (RWA) are the most critical and most studied micro-vibrations source [17, 18, 19]. The reason is that these devices induce a broadband vibration spectrum, and as main actuators of the ADCS, their continued activity is required during the pointing, acquisition and tracking phases. Thus, these disturbances cannot be neglected and their mitigation is needed in order to operate susceptible payloads as FSO Communication ones. The origins of the disturbance in a RWA are multiple, such as static and dynamic imbalance of the wheel itself, bearings imperfection and ripple from the electric motor, a cross-section of the RWA is shown in Fig. 2.3.
As discussed in the next chapters, when it comes to damping devices and system-level approach to micro-vibrations attenuation, RWAs are the main concern for engineers and researchers.

Cryo-coolers

Some payloads, such as hyper-spectral imagers, might need a cryo-cooler to support the low-temperature operation. The device is expected to function during nominal payload operations. The reason of this vibrations is mainly the

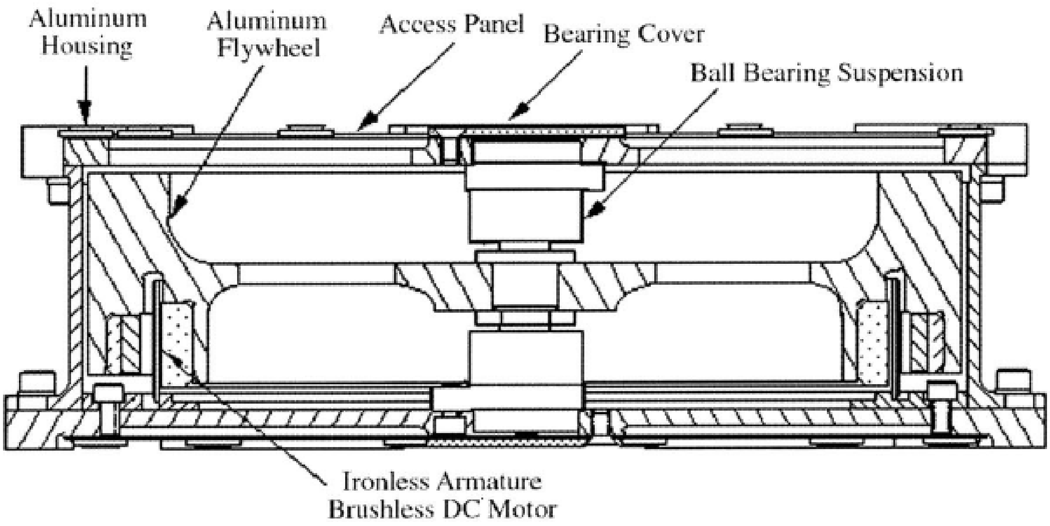

Figure 2.3: Cross-section of a reaction wheel assembly [18].

movement of the piston in the compressor. The main criticality about the cryo-cooler is its need to be in the physical proximity of the payload: this means that solutions such as load path dispersion or any accommodation-driven approach is not viable or limited. For reference, physical model and related schematic design is shown in Fig. 2.4

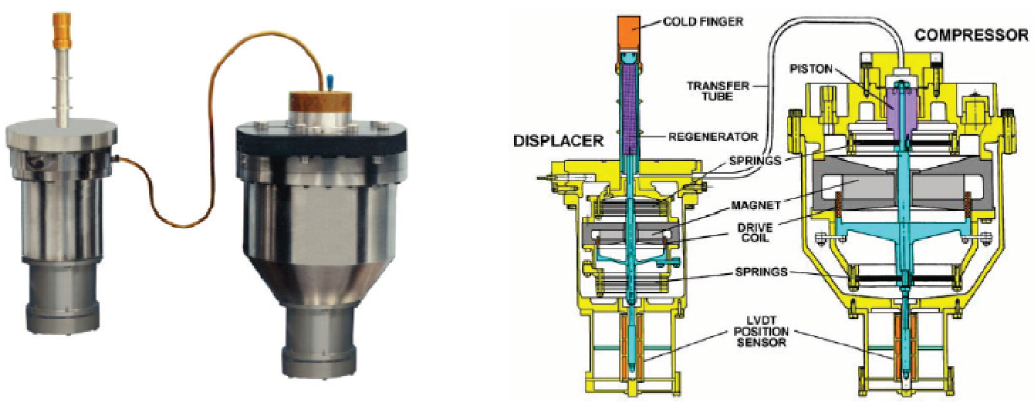

Figure 2.4: Typical design of a cryo-cooler [12].

Thrusters

When in orbit, spacecrafts require Station Keeping (SK) manoeuvres to maintain orbital parameters during their lifetime or a relative position with respect to Earth. SK manoeuvres are performed via the propulsion subsystem, mainly composed by tanks and thrusters.
The propulsion subsystem, mostly when it involves chemical thrusters and gimbals in general, induce a high level of micro-vibrations. However, this subsystem acts in a deterministic way, so that necessary firings of the thrusters happen at a known, certain time. This can help to design countermeasures on an operative level of the satellite, for example shutting down the communication during the thruster firing. In Fig. 2.5 a render of a chemical propulsion system is shown.

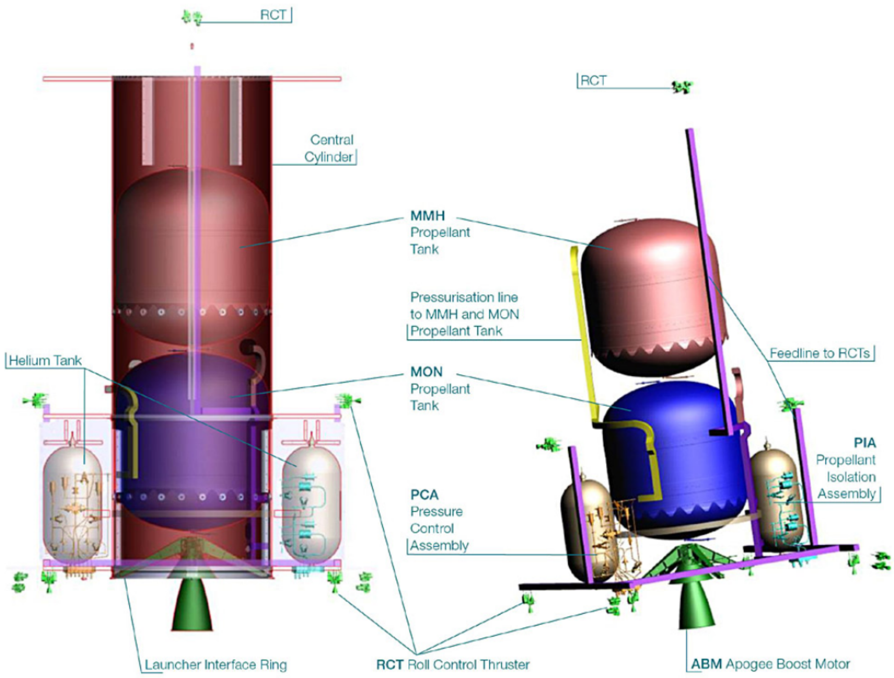

Figure 2.5: Render of a spacecraft propulsion system [image credit: Arianegroup].

Solar array and antenna drives

Steerable components such as solar arrays or antennas are usually driven by stepper motors. These devices, along with the mechanical response of these appendages, might introduce micro-vibrations of relevant magnitude. In a similar way to propulsion subsystem, the activation of these devices along the orbit and during the spacecraft schedule is known, so that operative countermeasures can be considered. In Fig. 2.6 a solar array drive motor is shown.

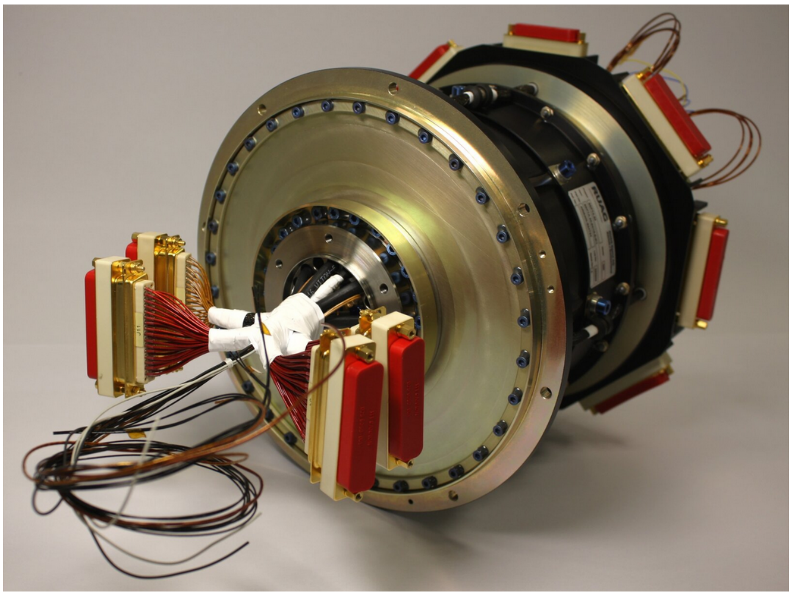

Figure 2.6: Solar array drive motor [image credit: ESA].

Other sources

Other disturbances might occur, induced for instance by the structural frame of the spacecraft. The thermal cycles the spacecraft goes through during his operating lifetime, mainly due to passages between solar exposure and eclipses, make the structure store some stress, that will be eventually released. This phenomenon is called sudden structural stress release. The structure will snap as the accumulated tension is released, and the mechanical solicitation will be dissipated through the structure itself. This phenomenon cannot really be controlled in any way, it is more regarded as an event that will occasionally happen.
Other clank phenomena might be induced by electro-magnetic effects from electric harness, or crackling of the multi-layer insulation (MLI) foils. These phenomena are anyway of much smaller entity with respect to aforementioned sources.

2.4 Micro-vibration space measurements

In order to develop an effective and reliable control system for the pointing requirements, Micro-vibrations measurements performed in the real space environment are critical to understand the behaviour of the satellite and the magnitude of the combined sources in nominal conditions. First studies performed by ESA on micro-vibrations related to future optical missions can be traced back to late 1980s.

2.4.1 Olympus mission

The Olympus-1 spacecraft was a communication satellite built for ESA, put in GEO orbit in 1989. The satellite weighed around 2.5 tons with a volume of 2.9 x 2.7 x 5.5 m, without considering solar panels.

Figure 2.7: Olympus satellite in preparation for launch [image credit: ESA].

Besides its main communication payload, the level of on-board micro-vibrations was investigated [20]. The measurement was performed via three orthogonal accelerometers, with a range of ± 100 mg and a resolution of 5 μg, in a frequency range from 0.5 Hz to 1 kHz. The accelerometers were mounted at the interface between the platform and the payload.
The measurements output was a linear acceleration. These measurements were converted in rotational accelerations assuming an infinite stiffness of the rotating body. The PSD obtained in this way is reported in fig. 2.8. It can be observed that the PSD rolls off with approximately 3dB/octave or 10dB/decade, in the

bandwidth from 1 to 500 Hz.

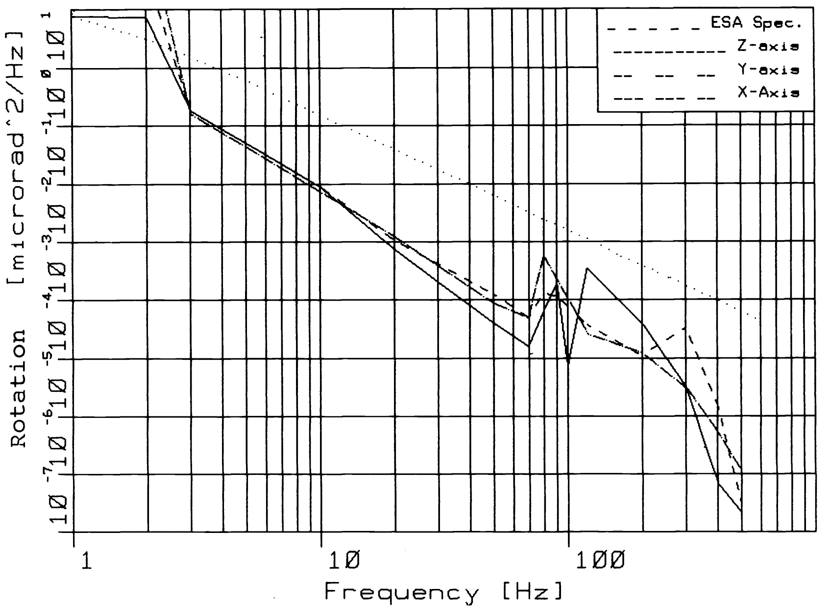

Figure 2.8: Angular acceleration of the Olympus spacecraft [20].

The PSD slope is in accordance with the ESA specification envisioned for the SILEX optical communication payload, that was bound to be developed in the next years:

$$S(f) = \frac{160\ \mu\text{rad}^2/\text{Hz}}{1 + (f/1\text{Hz})^2} \tag{2.4}$$

Besides "static" operation conditions, other micro-vibration data have been reported, as during thruster firing for station keeping manoeuvres (fig. 2.9), and during the activation of the Solar Array Drive Mechanisms (SADM) (fig. 2.10); the latter causes a disturbance phenomenon at about 300 Hz, due to the interaction between the motor and the ministep electronic. The two combined effects are combined and analyzed in fig. 2.11.

This analysis showed how, despite micro-vibration levels are well managed during coasting, when thrusters and SADM are activated the disturbances increase and exceed the specifications level. This suggests that careful approaches are needed for on-orbit operations, as these could induce unacceptable jitter.

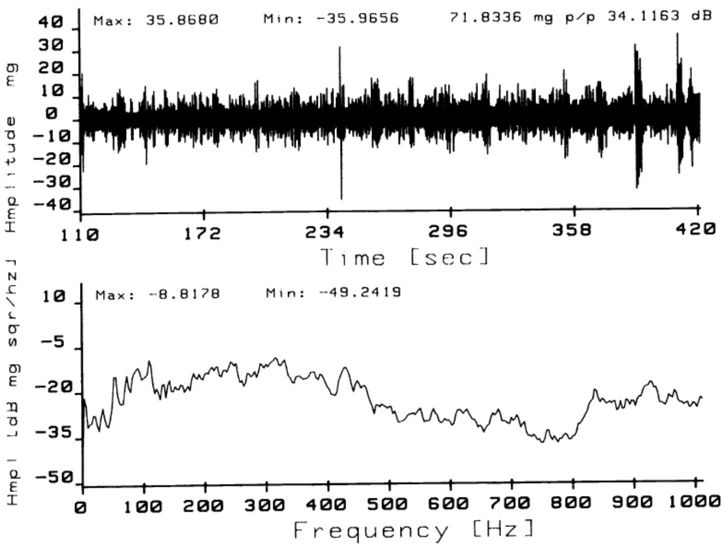

Figure 2.9: Thruster firing during Station Keeping manoeuvre [20].

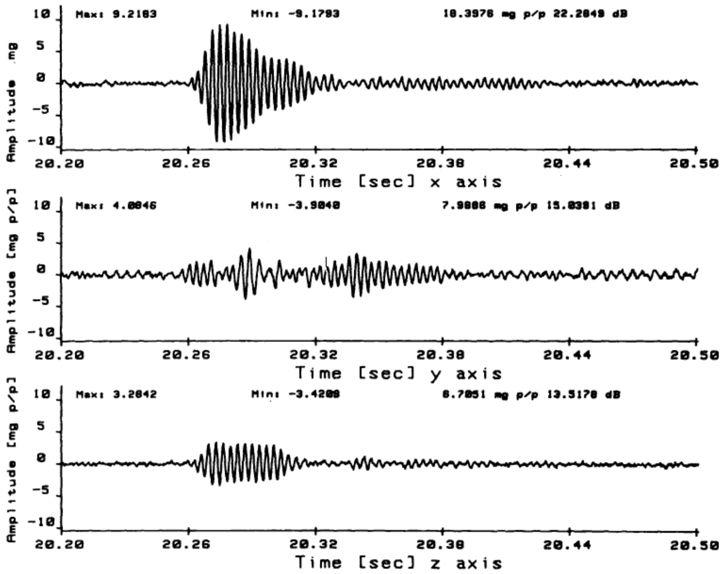

Figure 2.10: Time-domain disturbances induced by SADM [20].

2.4.2 OICETS

Relevant micro-vibration measurements were performed on board of the OICETS spacecraft developed by JAXA in 2005[16]. OICETS was part of a demonstration mission for interorbital optical communication; put in LEO orbit, it performed optical communication links with ARTEMIS GEO spacecraft. It

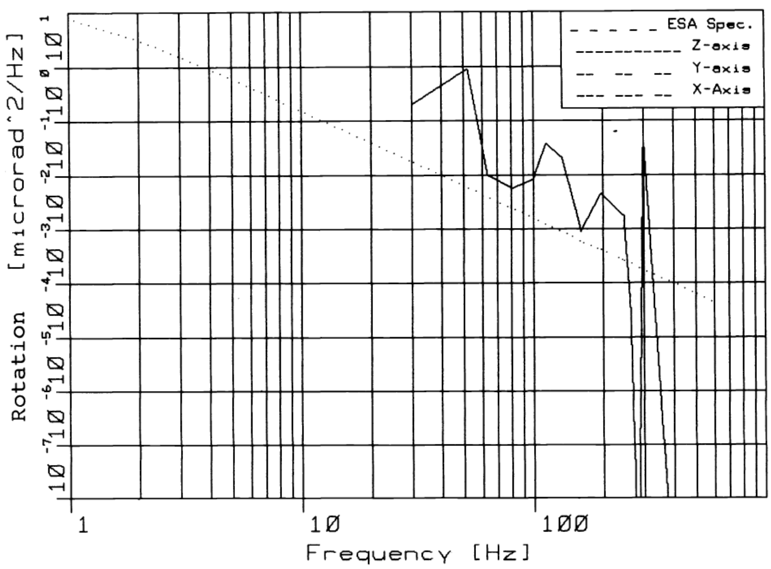

Figure 2.11: PSD of the combined thruster and SADM disturbances [20].

had a "box-wing" bus with a size of 0.78 x 1.1 x 1.5 m and a mass of 570 kg. This experiment allowed to evaluate a real micro-vibration spectrum for a spacecraft mounting an optical communication payload. Although it was mentioned that the spacecraft would primarily serve for LEO-to-GEO link experiments, the measurements performed took place during LEO-to-ground laser communications. The accelerometers were put at the interface between the platform and the payload, as shown in 2.12.

Accelerometers had a sensitivity of 50 μG and a dynamic range of 100 mG. The accelerations of interest for the beam wander are of course the x- and the y-axis of the satellite body, as the beam direction is given by the z-axis. In 2.13 frequency spectra of the accelerations sensed during payload gimbal slewing and tracking can be observed.

These axial measurements can be translated in angular accelerations, and from here a PSD can be retrieved in order to evaluate the angular displacement of the z-axis from the desired position. In fig. 2.14 PSDs for both the tracking and the slewing cases are shown. Moreover, they are compared with other space measurements (such as the aforementioned OLYMPUS satellite) and with both ESA and NASDA specifications.

The rms value of the interface base motion was calculated for both cases: for tracking the rms was evaluated around 23.8 μrad, while for slewing around 43.8

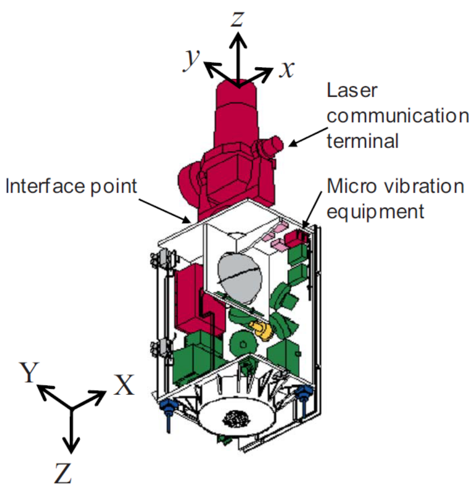

Figure 2.12: OICETS satellite scheme [16].

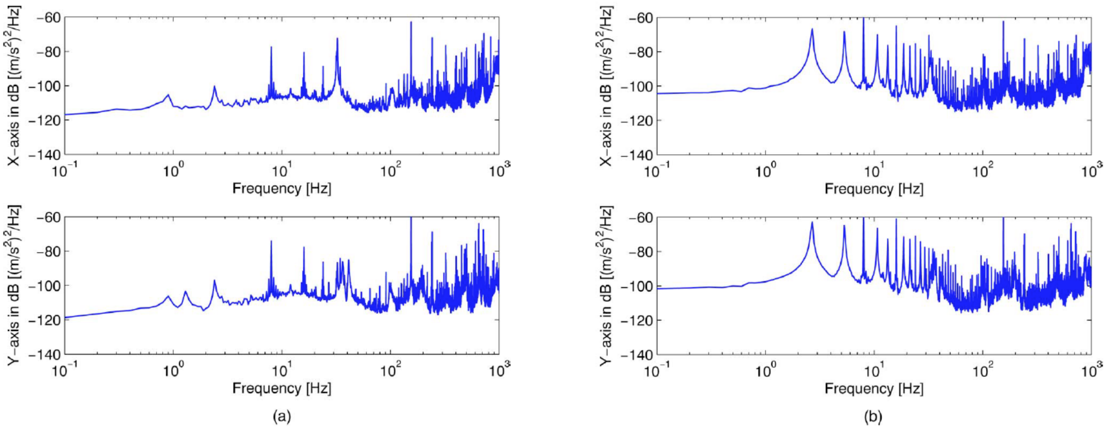

Figure 2.13: Frequency spectra of the accelerations sensed during (a) tracking and (b) slewing performed by the optical payload [16].

μrad, both in the 1-1024 Hz range.

It is also interesting to break down the frequency components of the PSD, as shown in Table 2.2. It can be seen how more than 90% of the base motion is stored in the 1-10 Hz frequency band, for both cases.

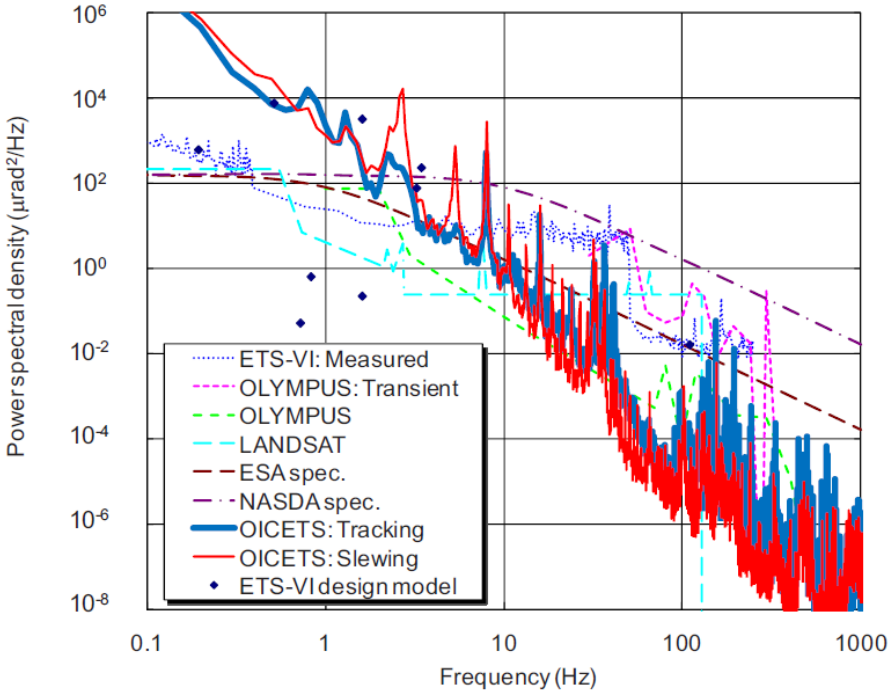

Figure 2.14: OICETS pointing disturbance PSD compared with previous data and specifications [16].

Frequency band	Tracking rms [μrad]	Band %	Slewing rms [μrad]	Band %
1 - 10 Hz	22.0	92.8	41.5	94.9
10 - 100 Hz	1.6	6.9	2.2	5.1
100 - 1024 Hz	0.1	0.3	0.0	0.0
Total	23.8	100	43.8	100

Table 2.2: Frequency band distribution of the disturbances [16].

2.5 Jitter emulation experiment

A preliminary experiment at the Institute for Navigation and Communication of the German Aerospace Center was developed, in order to obtain a first evaluation of the jitter effect at the receiver during inter-satellite optical link. The measurement was conducted in the frame of a series of experiments between two optical terminals in the close field range.

2.5.1 Setup

The setup of the experiment in terms of hardware was composed by two self-developed optical terminals [21, 22], which were put on a distance of about 30 meters. The micro-vibrations effects were simulated by feeding a .wav stereo signal in the Point-Ahead Angle mirror (PAA) of the transmitter terminal. The signal could then drive the PAA in the two axes and so emulate the beam jitter.

2.5.2 ESA model simulation

A micro-vibration model was developed in order to simulate the disturbances the payload can experience in space, and their effects on the communication performances. More specifically, the model considered was the one used by ESA for its micro-vibration specifications, the so-called ESA model. This model PSD is here reported in Eq. 2.5.

$$S(f)_{ESA} = \frac{2\theta_{rms}^2}{\pi\left[1 + \left(\frac{f}{f_{cutoff}}\right)^2\right]} \tag{2.5}$$

θ_{rms} is the rms value of the angular displacement from the desired pointing axis, while f_{cutoff} is the cutoff frequency from which the PSD starts rolling off.

The model was used as the reference to generate the .wav signal to be fed in the pointing system. The signal generator was developed in Python 3.7. The main idea for the development of the disturbance signal was starting from a Additive Gaussian White Noise (AGWN) and filter it to obtain the desired PSD shape.
The algorithm structure is as follows:

1. At first a zero-mean AGWN signal in the time domain is generated, with the desired angular rms value. This would generate a flat PSD, as the signal has the same magnitude in every frequency band.

2. The signal is then brought in frequency domain through a Fast-Fourier-Transform (FFT).

3. At this step the frequency shaping takes place. This is performed by multiplying the amplitude at each frequency, obtained from the Fourier Transform, by the square root of the ESA PSD, normalized by the numerator, as the θ_{rms} value was already specified in the WGN generation. The reason why the shaping is performed with the square root of the PSD is because of the relation between power, described by the PSD itself, and amplitude, which

is the value retrieved through the Fourier transform. The reason why this approach is possible is because we are investigating and ergodic process.

4. The signal is brought back in the time domain by an inverse Fourier transform.

5. The signal is then sampled at a frequency of 1 KHz in the .wav format (16-bit resolution).

6. The same process is repeated for the second .wav channel, in order to create the stereo .wav signal.

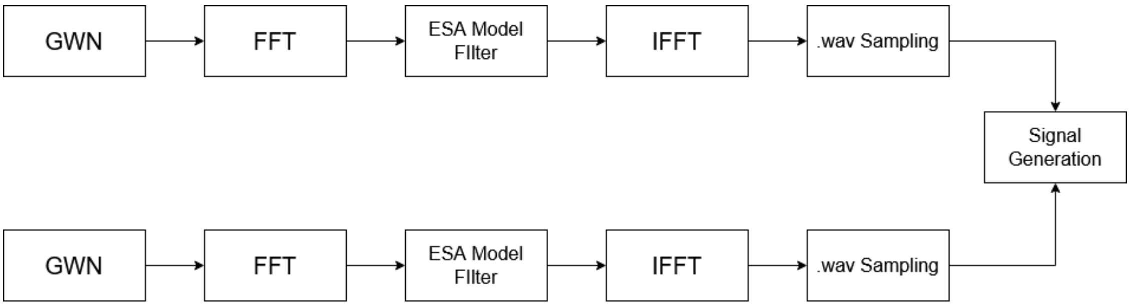

Figure 2.15: Flowchart of the signal generation code.

For the experiment, a θ_{rms} value equal to 20 μrad was chosen, and the f_{cutoff} set at 1 Hz. The signal was scaled to the terminal's mechanics and optics to produce the required ex-aperture pointing jitter. This step took place in the terminal's control software, hence the actual rms amplitude of the signal was 0.1. The PSD of the generated signal, compared with the ESA model, is shown in Fig. 2.16. The computed distribution is the one given by the combination of the two perpendicular signal vectors (i.e. the two channels) x and y, hence a vector $r = \sqrt{x^2 + y^2}$ is obtained. This means that the two identical gaussian distributed signals will eventually generate a Rayleigh distribution. It can be seen that despite the ripples (due to numerical integration error in the PSD calculation), the signal fits the desired specification accordingly.

To provide further visualization, a projection of the error cone is shown in Fig. 2.17, in the form of an histogram. The darker the zone, the more signal values are repeated there. As expected, the error distribution is way more dense in the proximity of the center (i.e. the pointing axis) also because of the reduced circular area with respect to higher radii, so that it is easier for values to overlap and be repeated. The rms value has been computed and highlighted with a green circle. As can be seen, it fits the 0.1 radius mark.

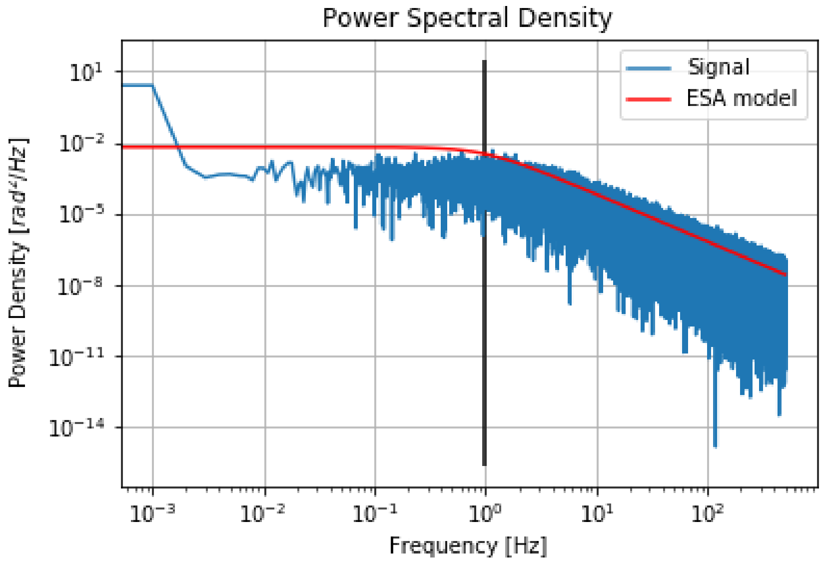

Figure 2.16: PSD of the stereo signal, compared with expected value from ESA Model.

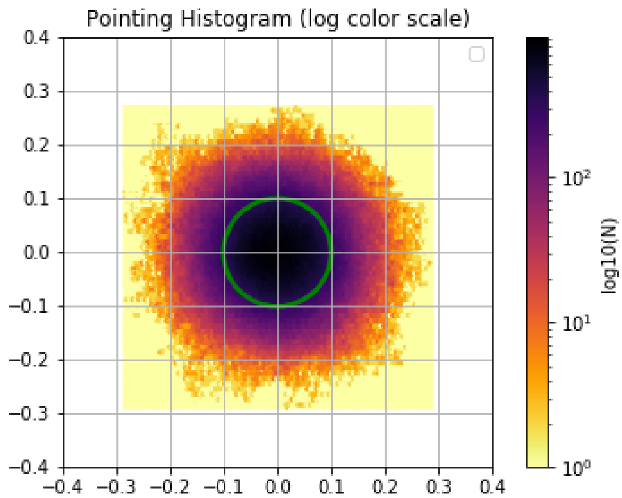

Figure 2.17: Simulated receiver plan histogram, with green circle representing the rms value.

2.5.3 Results

The artificial beam jitter causes signal fluctuations (in terms of optical power) at the receiving terminal. Due to the nature of the experiment, the influence

of the beam jitter was evaluated in terms of Allan Deviation [21], first in the terminal itself, then in 30-meter transmitter-to-receiver test. Although, the high-frequency jitter are integrated in the first (1-s) sample of the analysis, hence higher frequencies effects could not have been really evaluated, and all of the jitter effects can be considered to be condensed in the 1 second long sample.
In Fig. 2.18 results of the emulated jitter are compared to different cases.
Magenta line shows the Allan Deviation (ADEV) for a light signal reflected on the same terminal (back-to-back, B2B), with no jitter and no compensation (FSM open).
The yellow curve presents the same B2B measurement, but this time there is a jitter induced by the external mirror that reflects the light in the terminal, with a rms value of 25 μrad. This effect can be seen in the 1-second sample, which shows a higher deviation value.
The blue plot shows the FSO link between the two terminals, at a distance of 30 metres, plus 180 metres of optical fibre. In this measurement no jitter was induced, although the overall stability decreases due to the link configuration and instability in the fibre.
Finally, the red line shows the FSO link with the ESA model jitter induced, with a rms value of 20 μrad. The ADEV value is the highest compared to the previous cases. This leads to an interesting result for the representation of an inter-satellite link, although being in the near-field range. Next steps will involve:

- the acquisition of the jitter signal on the receiving terminal;
- optimisation of the jitter model for the repetition of the signal sequence, in order to run longer tests with no problem during the rerun of the .wav file;
- enhancement in the stability of the optical components (i.e. fibre damping) and electronics;
- a far-field test on a longer distance.

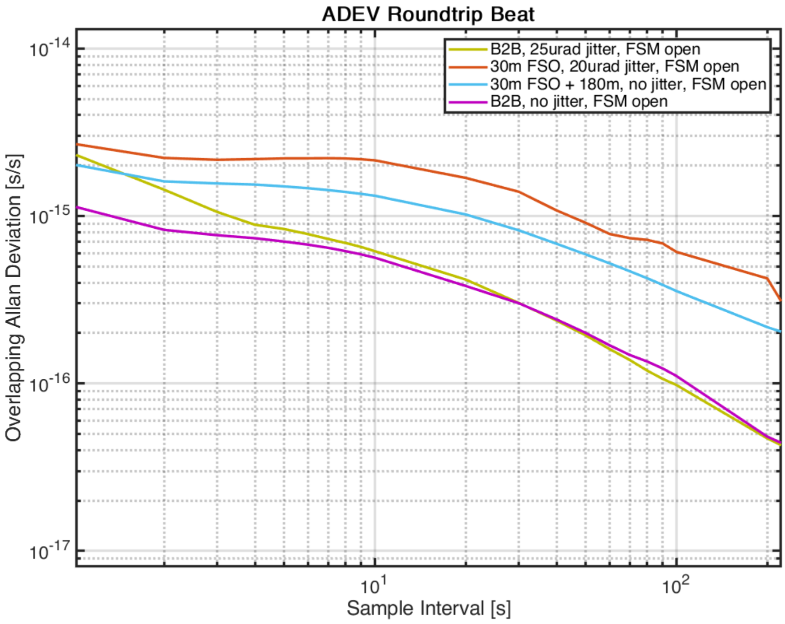

Figure 2.18: Experiment results.

Chapter 3

Damping and Compensation Approaches

As seen in the prior chapter, the micro-vibration environment the payload faces might severely compromise the mission if not carefully managed. Several techniques and technologies have been developed to effectively counteract micro-vibrations coming from internal sources. These can be split in two main approach categories: damping and compensation.
Damping techniques involve the application of mechanical isolators across the spacecraft, usually in proximity of critical vibration sources or sensitive payloads. The goal is, intuitively, to minimize the transfer of disturbance from sources to payloads.
Compensation techniques are related to active mechanisms present in the payload. In order to achieve the μrad order of precision, these systems are necessary, and are involved in every FSO communication payload. These usually consist of mechanically driven mirrors inserted in the optical train.
Throughout the chapter, most common damping and compensation approaches are analysed and discussed, with some considerations about upcoming new technologies and solutions.

3.1 Damping approach

When first considerations about micro-vibrational environment were made, it appeared clear how the main concern for upcoming missions was to minimise the disturbances. Even though some intrinsic aspects could be enhanced, e.g. a more balanced reaction wheel assembly, a base magnitude of micro-vibrations still remains, and needs to be taken care of. For this reason, damping approaches

started gaining popularity for solving this criticality.
This approach involves the use of isolation technologies, such as passive elastomer components, springs, or more elaborate systems as active mechanical isolators and hybrid (i.e. half passive half active) isolators. In Fig. 3.1 it is reported a visualization of the relationship between reaction wheel disturbances, the spacecraft structural dynamics domain and the isolation countermeasure with respect to frequency region.
In case of very low frequency, which is out of the scope of this thesis, the ADCS control can easily balance these disturbances. This was already discussed in Ch. 2, where the disturbance sources have been discussed: in low frequency region usually external disturbances, such as solar pressure and gravity gradient, are more relevant, whilst internal disturbances are not as critical.
Passive isolators are involved in the higher frequency band damping, the region deemed to be critical for our study. Here main disturbance harmonics lie, as well as higher order harmonics. This applies not only to reaction wheels, but to other internal disturbances discussed before, such as stepper drivers and cryo-coolers.
Active isolators are usually involved in the frequency region between the two aforementioned frequency bands.

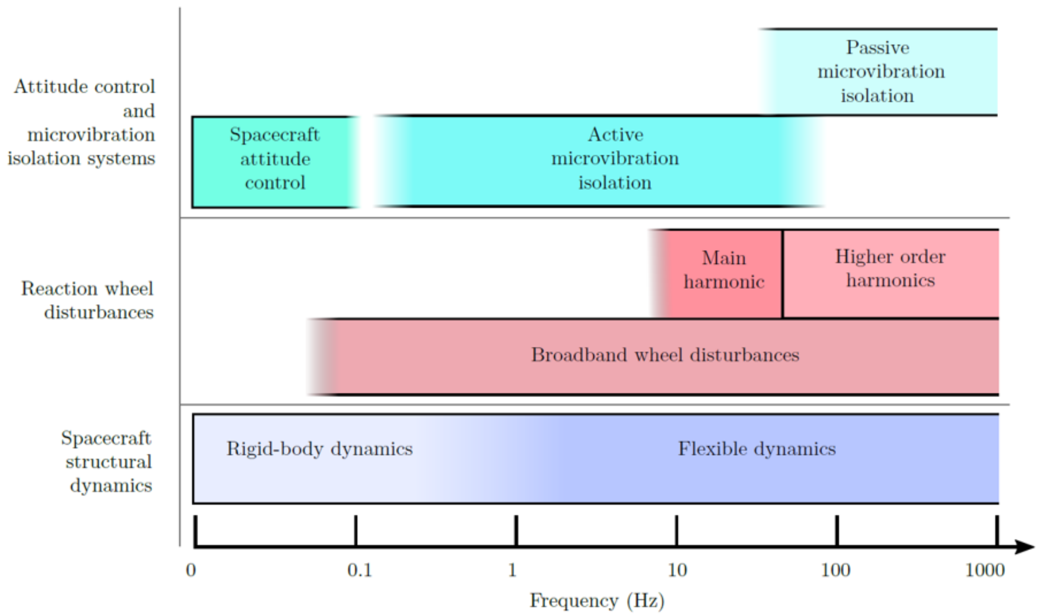

Figure 3.1: Micro-vibration disturbance range and related countermeasures [17].

3.1.1 Passive Isolators

Passive isolators are the most common and mature solution for disturbance damping, and are generally to be preferred for multiple reasons. First of all, when it comes to space systems design in general, fault tolerance is a key driver. Intuitively, passive isolators are definitely less likely to experience a failure with respect to more complex active and hybrid solutions. Moreover, these solutions are definitely more compact, cheaper and less power demanding with respect to the aforementioned counterparts.

Passive isolators can be modelled as mass-spring-damper mechanical systems. This allows to capture main mechanical characteristics such as natural frequency and damping ratio. The mechanical model can be summarized by the equations system in 3.1:

$$\begin{cases} m\ddot{x} + c\dot{x} + kx = F \\ c\dot{x} + kx = F_t \end{cases} \tag{3.1}$$

The system is governed by the transfer function in Eq. 3.2:

$$H(s) = \frac{F_t}{F} = \frac{cs + k}{ms^2 + cs + k} \tag{3.2}$$

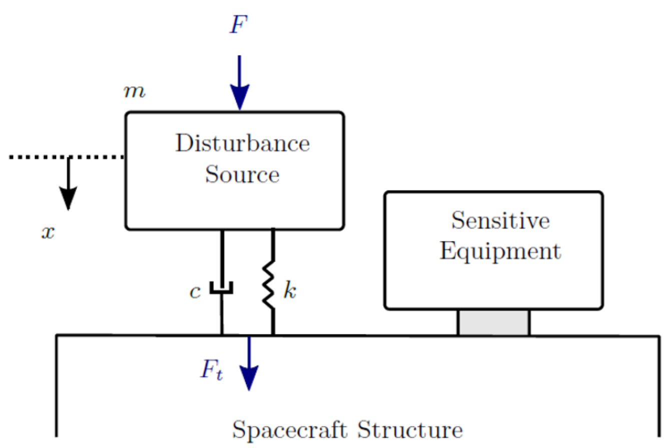

Figure 3.2: Passive isolator in the source-to-platform configuration scheme [17].

The natural frequency is defined as $\omega_n = \sqrt{\frac{k}{m}}$, and it is the frequency at which the system will oscillate without any damping effect. The damping ratio is defined as $\zeta = \frac{c}{2\sqrt{mk}}$, and as the name can suggest it defines the damping capabilities of the isolation device. In Fig. 3.3 it is shown how, given the same values for the mass m and stiffness k, the response of transfer function in Eq. 3.2

changes with different damping c values. With a null c value, the response past the ω_n peak at 10 Hz decrease in a steep way. Increasing the c value, it can be seen how the peak is flattened, but this is paid with having a higher magnitude response at higher frequencies. This trade-off between peak response and higher frequency response characterise most passive isolators.
As a consequence, performance limitations of passive isolators in the low frequency region appear evident, along with concerning response peaks in the proximity of the natural frequency. Nevertheless, the good rejection capabilities in the broader and higher frequency region make this type of isolators the baseline solution, from which the rest of the damping and compensation framework can be built.

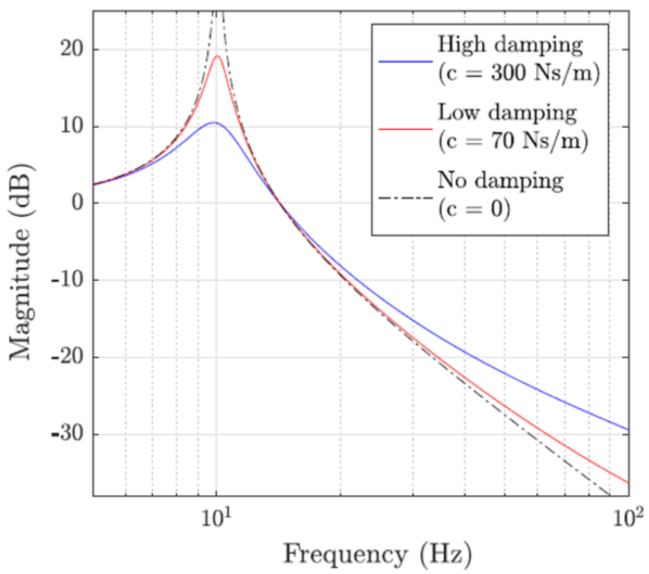

Figure 3.3: Comparison between different damping magnitudes in passive isolation devices [17].

Reaction Wheels Isolators

As already mentioned, reaction wheels are the most critical disturbance sources, hence this actuators are usually the most addressed components when it comes to passive isolation. The rejection capability of passive isolators in the high frequency range fits well with the broad bandwidth of the vibrations induced by the wheels. For this reason, reaction wheel isolators are one of the most common solutions to first provide a more stable platform. One of the most notorious showcase of such technology was Hubble Space Telescope [23], which used passive isolators on RWA's to achieve a quieter micro-vibration environment.

Most common passive isolators use visco-elastic springs as their core. Depending on the spacecraft necessities and capabilities, a single device can isolate all the RWA's involved, address them one by one (i.e. one isolator per wheel) or a hybrid solution.
As for single-wheel isolation devices, an interesting example can be given by [24]. This solution consists of a flexible platform composed by folded beams, that connect the disturbance source to the main structure. This platform aims to optimise the trade-off between sufficient static stiffness, to support the mass of the reaction wheel, and minimum dynamic stiffness, using a lightweight solution. The flexible beams are then attached to a stiffened base, for proper installation on board. In fig 3.4, 3.5 the device scheme and the full realised system can be seen, respectively.

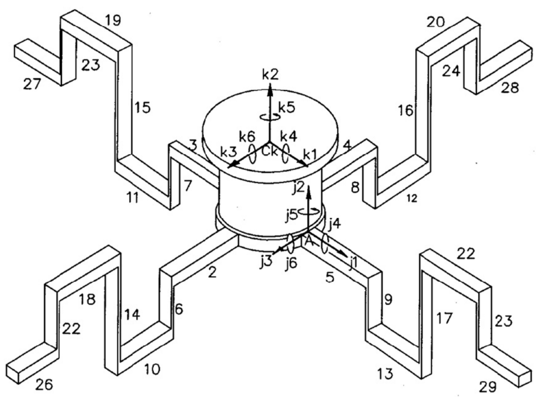

Figure 3.4: Schematic design of the RWA passive isolation system [24].

In fig 3.6 performances of the isolation device are shown. Comparing non-isolated disturbance forces (on the left) with the isolated ones (on the right), it can be seen how most of the disturbance peaks in the high frequency region are damped, only leaving peaks in the low frequency range, as a consequence of what has been already discussed earlier in this chapter. This holds for the whole wheel spin rate considered.

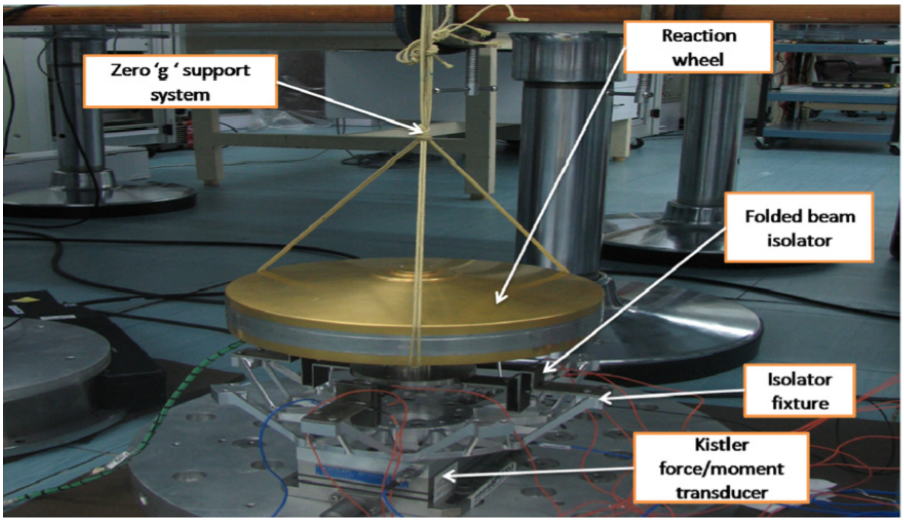

Figure 3.5: Realization of the RWA passive isolation system [24].

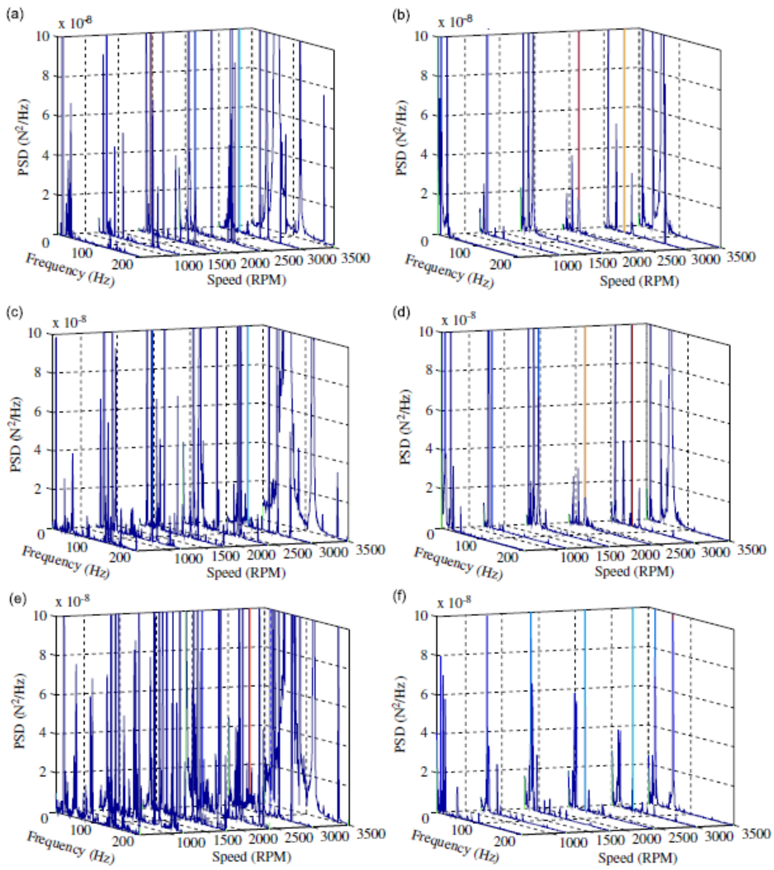

Figure 3.6: RWA passive isolation system performances. Left: disturbance without isolator. Right: disturbance with isolator employed [24].

A clarifying example for a device involving all the wheels is the isolation system employed in [25]. This system also takes in account the damping of loads experienced during launch phase. Although magnitude and frequency involved during this phase are different from the ones of interest from our study, it has been discussed in [26] how damping launch loads can be beneficial for micro-vibration performances during operating life of the RWA system.
A schematic view of the system can be seen in Fig. 3.7. The four wheels employed in the ADCS are paired in two separate carbon fiber braces. The braces are connected to the visco-elastic springs, that act as the main isolators for the disturbances. The springs are then connected to a stiffened panel, called Mu-panel, that is tuned in order to avoid structural coupling with the main spacecraft structure, to which the panel is connected via the Space Facing Facet (SFF). Beneath the Mu-panel there are the lockdown springs, that are employed for damping the launch loads and thus obtain a better micro-vibration performance of the wheels.
For each brace a radiator panel was directly attached to the bottom part, in order to keep the RWA in the proper operating temperature range. This brings the advantage of eliminating the thermal straps, that could act as mechanical load path and bypass the springs damping. In Fig. 3.8 the real hardware can be seen.

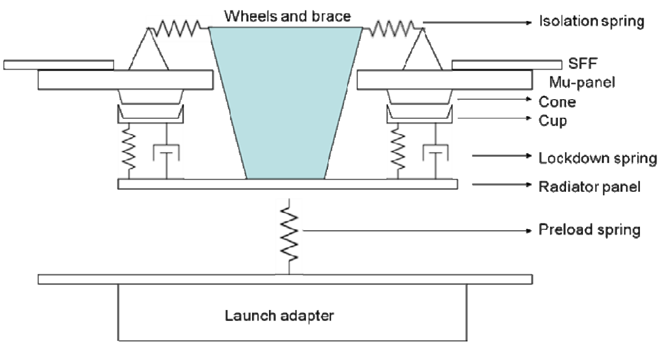

Figure 3.7: Design of the isolation system for a wheel pair [25].

The employment of such a system can greatly benefit the overall spacecraft micro-vibration environment. To give a quantitative performance of the system, in Fig. 3.9 a performance graph is shown. Most relevant plots in the graph are the blue curve and black curve: blue one represents a single reaction wheel in the 100-2000 rpm speed range, while black one represents a couple of isolated wheels in the same speed range. For completion purpose, red curve represents a single wheel in the 100-5000 rpm speed range, while green curve represents the background noise sensed by the Kistler table used for the measurements.

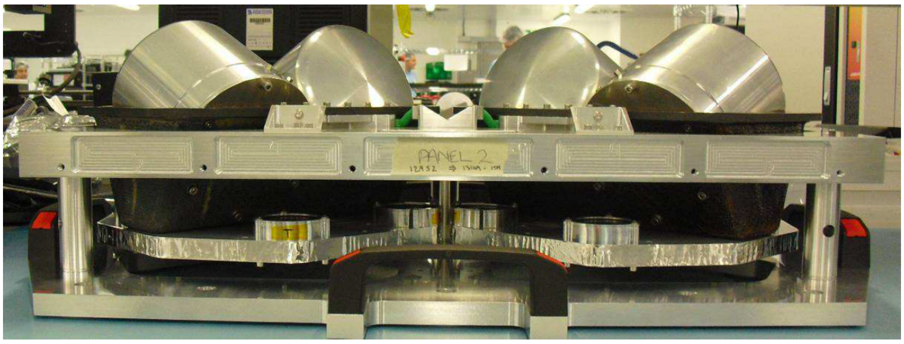

Figure 3.8: Hardware of the RWA passive isolation system [25].

Comparing blue and black curves, it is clear how the isolation system greatly reduces the disturbances. The PSDs of the isolated wheels show disturbances with two or three orders of magnitude lower than the non-isolated PSDs, for most of the frequency range. It is important once again to highlight how the isolated measurements encompass a set of two wheels, while the non-isolated ones are registered for a single wheel.

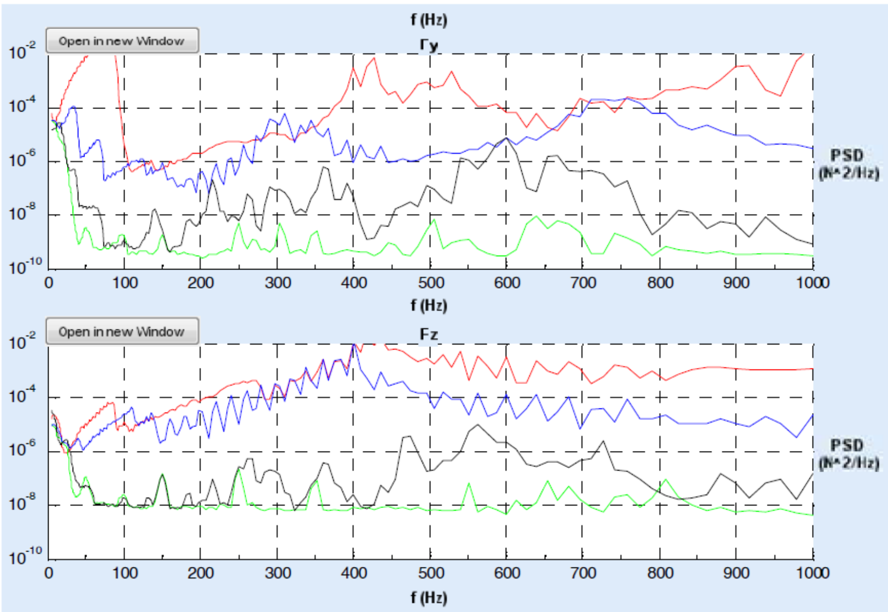

Figure 3.9: Performance of the encased wheels isolation system [25].

Solar array isolators

Solar arrays can induce micro-vibration disturbances too, as discussed in Ch. 2, although not as critical as the ones induced by RWA. Nevertheless, for high-precision pointing payloads this aspect should not be overlooked. In Hubble Space Telescope for example, despite having already on board RWA's isolators, it was decided to mount solar array dampers during Servicing Mission 3 [27], as new and more rigid solar arrays would be mounted in the same Servicing Mission. More rigid appendages would mean fundamental bending modes of higher frequency, in this case reaching the order of 1 Hz, not suitable with the pointing requirements of the Telescope.
The solution adopted was the integration of a damping system between the solar array mast and the solar array drive mechanism coupler, as can be seen in Fig. 3.10.

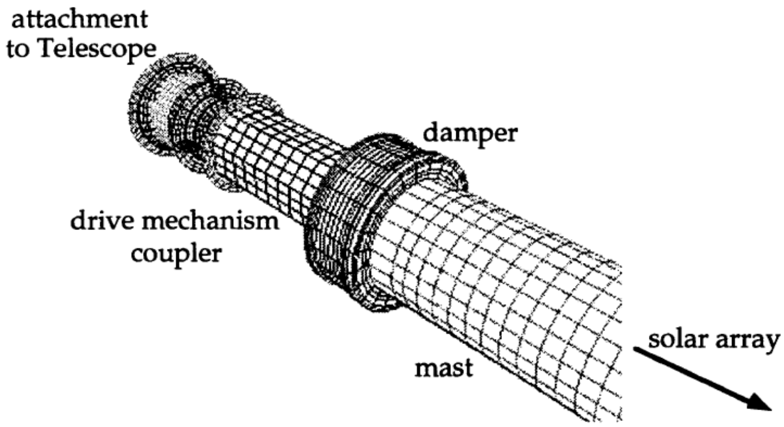

Figure 3.10: Solar array damper accommodation [27].

The damper was specifically designed for this application, and consists of a titanium alloy spool, around which shear laps are mounted, between the upper and the lower flanges of the spool. These shear laps are structured as a sandwich composition of a visco-elastic material (that enables the damping function of the isolator) between two titanium layers. The section of the damping spool is shown in Fig. 3.11. The titanium spool that provides the structural base of the damper was deemed necessary in order to meet the operating temperature range requirement, along with the high strength-to-weight ratio.

Payload Isolators

So far, passive source-to-platform isolation systems have been discussed. Nevertheless, passive payload-to-platform isolators are viable solutions too.

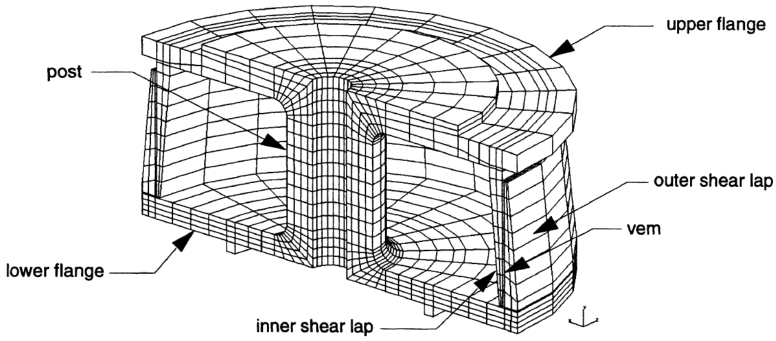

Figure 3.11: Cross-section of the damper spool [27].

EDRS-A mission approached this solution in order to accommodate the FSO communication payload on the spacecraft platform, as discussed in [8]. The optical payload is mounted on the Earth-pointing deck of the spacecraft, on top of an isolation system defined as Payload Elastomer Mounting System (PEMS). The PEMS consists of a rigid base mounted on top of the viscoelastic supports that act as dampers, which are connected via support brackets at the main spacecraft structure. The model of the PEMS, with LCT on top of that, is shown in Fig. 3.12. It is worth to mention the connection between the main payload frame and the spacecraft structure, designed so that necessary harnesses would not serve as a bypass for mechanical sollicitations. To do so, such harnesses were made flexible enough in order not to represent a risk for high frequency mechanical transmission. This was done for heat transfer pipes too, which connect the isolated LCT frame and the condenser plate mounted on the main structure, as shown in Fig. 3.13.

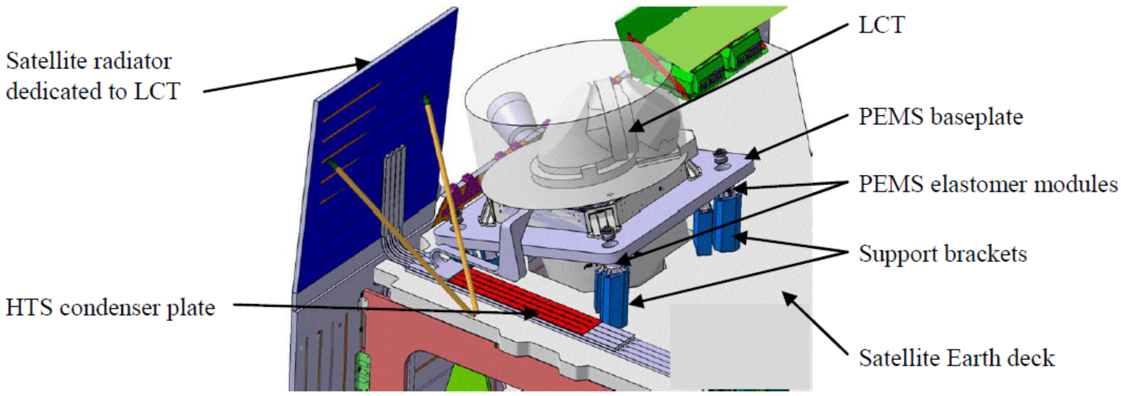

Figure 3.12: CAD model of PEMS with optical payload integrated [8].

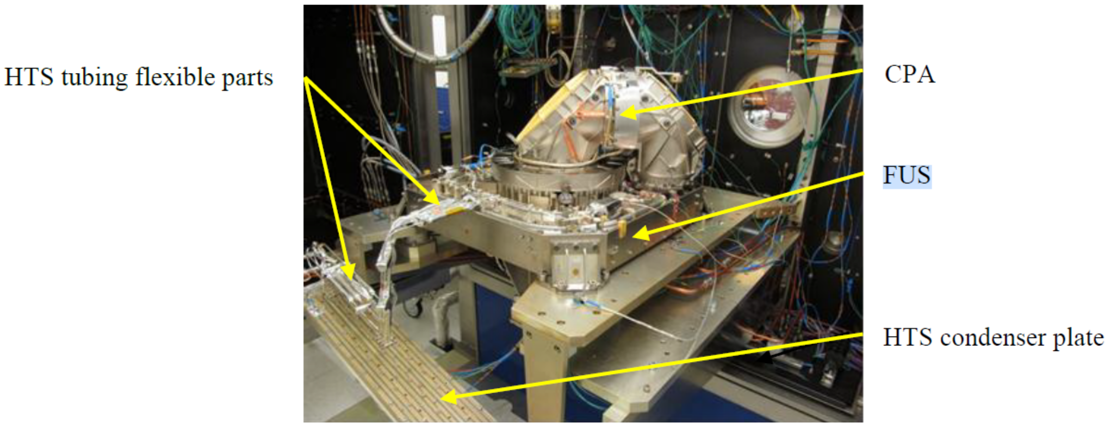

Figure 3.13: PEMS hardware, with highlighted harness [8].

Results of the vibration tests conducted on the isolation system are shown in Fig. 3.14. Dark blue curves represent the angular displacements measured without the isolator, while yellow and pink curves represent measurements obtained with the mechanical isolator employed. It can be seen how disturbances in the high frequency range are reduced by one to two orders of magnitude, while clearly introducing small peak disturbances in the lower range, as intrinsic consequence of employing a passive isolation system.

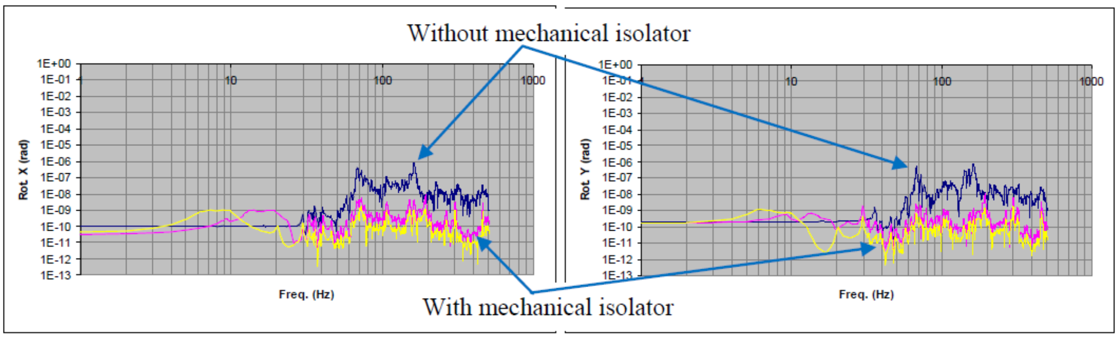

Figure 3.14: PEMS rejection performances [8].

3.1.2 Active Isolators

Active isolation systems involve the use of control loops through sensors and and actuators in order to provide force feedback signals and obtain a mechanically stable environment. As a functional scheme interpretation, as shown in Fig. 3.15, the system is a damp-spring-mass similar to the one already shown in Fig. 3.2, with the main difference relying in the capability of this system to actively tune damping and stiffness. This control can result in good performances regarding low frequency disturbance isolation.

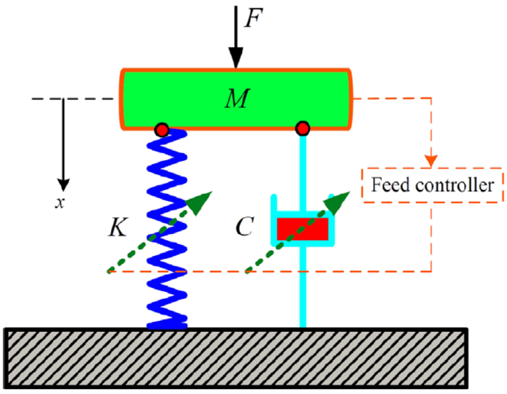

Figure 3.15: Active isolator functional scheme [28].

Control Techniques

Most common control techniques proposed for this type of isolators are positive position feedback (PPF) control and anti-phase control. This techniques commonly envision the use of piezo-ceramic wafers for sensing and actuation units.
As for PPF control, such technique is suitable when a narrow, low frequency band requires damping, hence it is usually considered when a dominant structural mode is critical and needs to be locally attenuated. Isolation performances of active damping can reach up to 10-20 dB for the best controlled modes, as discussed in [29]. Nevertheless, other modes remain almost not damped when positive position feedback control is used.
Another option is the anti-phase control, which is usually preferred when active damping is employed to locally isolate the sensitive payload from the noisy spacecraft environment. This type of control comes in handy when disturbance source is harmonic, as for example primary reaction wheel disturbance modes [30] or cryo-cooler pumps.

Some studies about control techniques involving neural network technology have been conducted too [31]. Advantages of such technique would be a responsive and adaptive control of the isolator to overcome eventual changes in the operating conditions (e.g. partial failure of the isolation system). It is noteworthy how the system was capable of fast control adaptation even starting from no or minimum prior knowledge and external training data. For reference, the neural network based control managed to perform a rejection of 25 to 55 dB in the 10-15 Hz range. Moreover, the control proved to be effective in the occasion of fault recovery modes, deactivating part of the actuators. This is interesting as one of the main concerns for active isolators is their adapting capability out of nominal operation conditions.

Stewart Platforms

Active isolation systems are usually envisioned to isolate the payload from the rest of the spacecraft, as seen in [29, 31]. The reason why is that such a complex device, capable of low frequency disturbances rejection, finds his most valuable application in close proximity of the sensitive payload to be isolated. These devices usually come in the form of Stewart Platforms (also called hexapods).
The Platform consists of three main parts: the base, the struts and the payload plate, to accommodate the instrument of interest. The base is rigidly attached to the main spacecraft structure, and acts as structural support for the struts and the payload. The struts are the components of the platform that enable the damping function: these are piezo-electric actuators that counteract disturbances coming from the base. Finally, the payload plate is where the instrument is rigidly mounted, taking advantage of the mechanically quieter environment provided by the platform. The advantage of this solution is also the capability of rejection for all the six degrees of freedom, thus potentially providing noise cancellation in every direction.
Considering again the discussion about control techniques, in case of failure of one of the struts (i.e. the strut remains blocked in a rigid position), a set of alternative control algorithms are needed for every fault recovery mode, in order to continue operating the mission even if in a degraded mode; or in alternative a neural network adaptive algorithm is needed, capable of changing control dynamics according to new input signals. In both cases, research and development effort is required to design not only a more complex hardware, but also to provide the proper control algorithms. When considering to employ an active isolation device, these aspects cannot be overlooked.

An example of the rejection performances, from a Stewart Platform tested in [32], is shown in Fig. 3.17, for the three orthogonal acceleration directions and for both frequency and time domain. The results show a good attenuation of the dominant structural modes, in the 100-200 Hz frequency range, for all

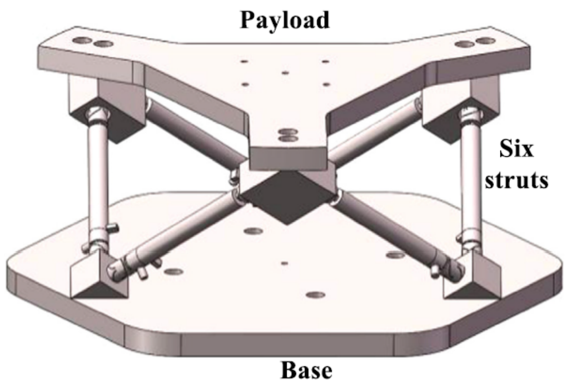

Figure 3.16: Stewart Platform design [32].

three components of acceleration. Attenuation rms values set around 10 dB with an exception for X-axis, where a 22 dB attenuation value is measured, due to a peculiar single-peak modal disturbance. The narrower the disturbance band, the better active isolation devices work.

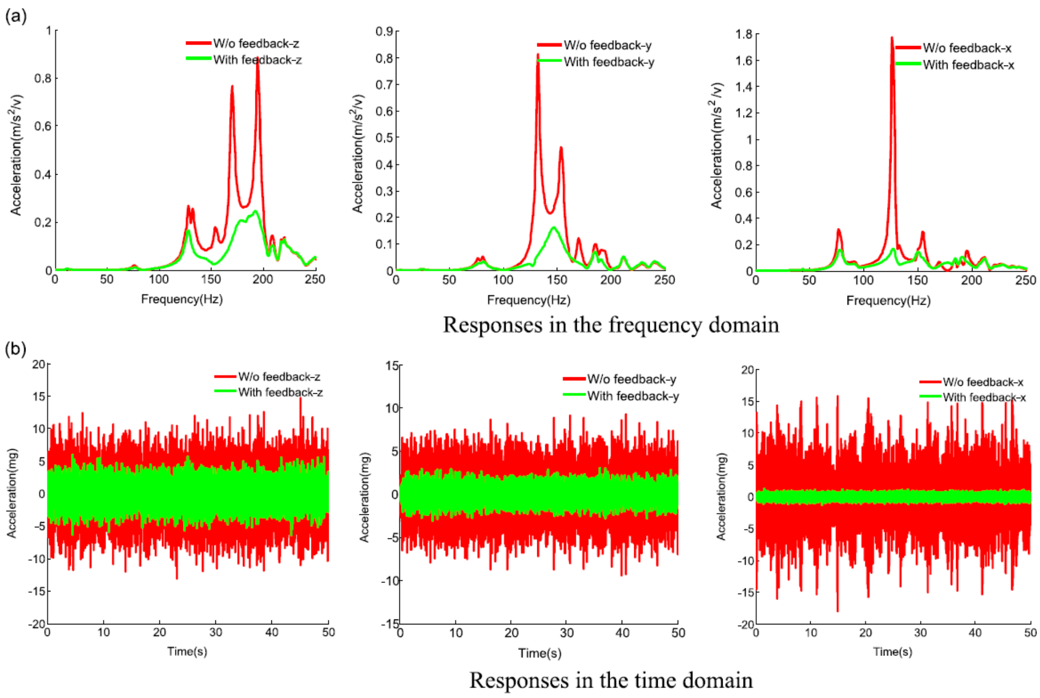

Figure 3.17: Stewart Platform rejection performances [32].

In conclusion, whilst active isolation can be useful to overcome low frequency disturbances, their employment implies an additional complexity to the whole spacecraft system. These isolators require power supply, thermal control and special structural mounting adaptation. Moreover, they are in general heavier and more complex systems (hence more subject to failure) with respect to passive isolators. These additional requirements, in turn of a benefit limited to a narrow bandwidth of disturbances, require a careful trade-off analysis.

3.1.3 Hybrid Isolators

Hybrid isolators aim to merge the advantages of passive and active isolators, attempting to minimise the respective drawbacks. As a concept, active components should address the low frequency range, while passive components should address broader and higher frequencies. Of course, employing active isolation requires all the efforts mentioned before (hardware, power supply, control loops), and an eventual failure of the active components would not inhibit the whole device, as passive components can still fulfil their function. These devices have been investigated in literature, with some of the most relevant results coming from [17, 33, 34].
The passive-active isolator developed in [33] is an interesting example of how a passive device can be modified to become hybrid. Folded beams, already introduced in Fig. 3.4, were modified applying piezo-ceramic components on the most flexible parts of each beam as shown in Fig. 3.18, in order to actively tune mechanical characteristics.

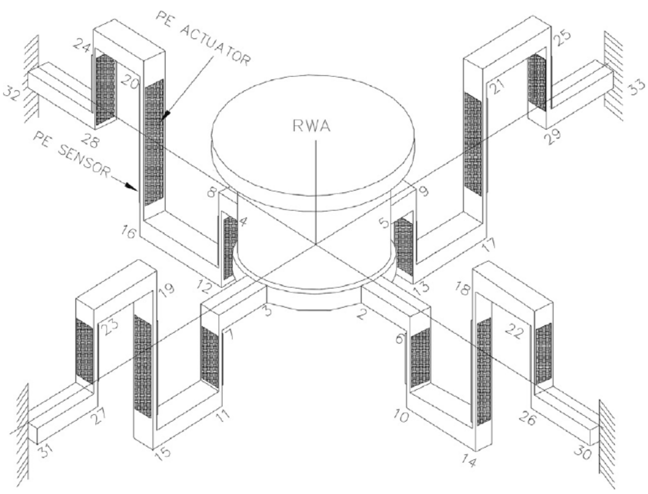

Figure 3.18: Hybrid folded beams isolator[33].

A popular solution for hybrid isolators envision the integration of passive isolation components on the struts of an hexapod platform. For instance, the Vibration Isolation and Suppression System (VISS) [34] includes a working viscous fluid for passive damping in each of the D-struts. VISS with integrated payload (left) and scheme of the single strut (right) are shown in Fig. 3.19. At the base of the strut, two primary bellows for the passive hydraulic system were implemented; on top of that, voice coil actuator is used for active functions of the isolator; on the bottom part, a preload spring is installed so that the hexapod will withstand launch loads. VISS was developed to accommodate a MWIR optical payload, and to specifically address vibration attenuation of the first three cryo-cooler harmonics (55, 110 and 165 Hz). Moreover, the platform was also required to perform accurate steering (±0.02ř) of the payload. Focusing on the vibration rejection capabilities of the isolator, in Fig. 3.20 a comparison between passive-only and active-passive suppression performances of the system in the low frequency range is presented. While passive-only performs well, it is clear how it is unable to counteract the first mode of the cryo-cooler, at 55 Hz. The activation of the control loop allows to enhance such performances and obtain an overall better rejection, with the 55 Hz peak suppressed. In general, the system was claimed to be able to provide an over 20 dB rejection at all frequencies above 5 Hz. VISS and its related payload were launched on board of the TSX-5 spacecraft in 2000, and proved full functionality of the isolation system.

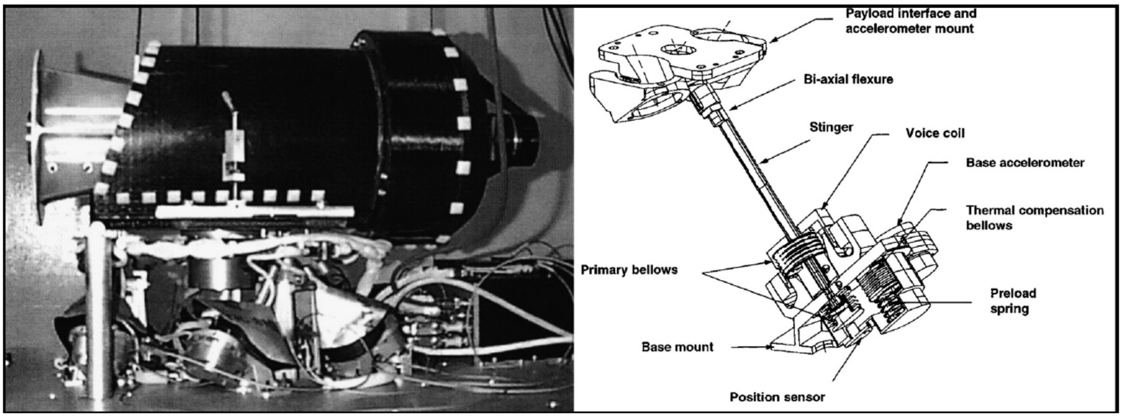

Figure 3.19: Left: VISS hexapod with payload on top. Right: scheme of the single strut [34].

Another, more recent concept for hybrid isolation was developed through [17, 35, 36, 37]. This device was developed in order to isolate the disturbance source (in the examined case the most common one, the reaction wheel) from the rest of the platform. Isolator scheme and its realization are shown in Fig. 3.21. The system is composed of an "active plate" that rigidly supports the source to be isolated. The plate is not active per se, as it is in fact controlled by six proof mass actuators, three on vertical axis and three on tangential axis. The

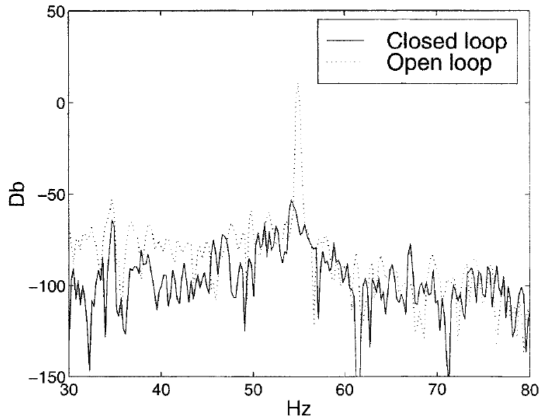

Figure 3.20: VISS low frequency rejection performance [34].

plate is mounted on top of four elastomer modules, which compose the passive component of the isolation system. Each elastomer is mounted on top of a force cell sensor: these sensors provide the feedback for the aforementioned actuators, in order to suppress the perturbations in the 10-50 Hz range.

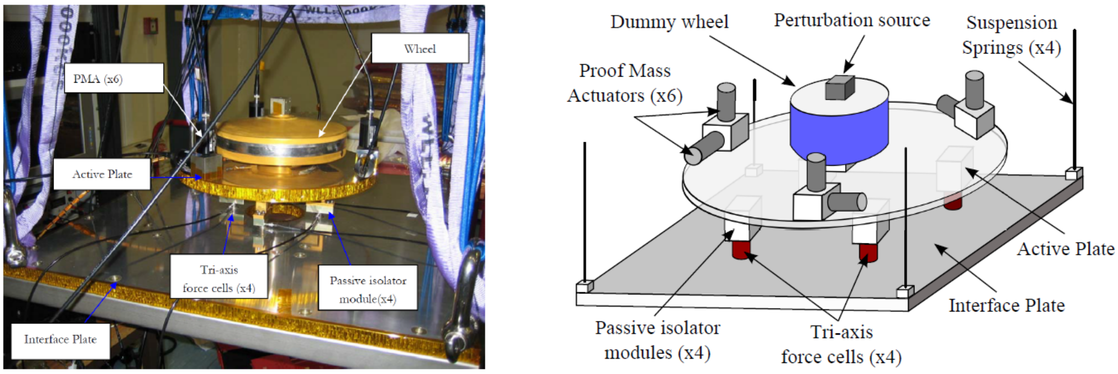

Figure 3.21: Hybrid isolator with active plate. Left: model realisation. Right: schematic view [17].

Results are shown in Fig. 3.22, showing PSD's of forces and torques signals. It can be appreciated how the rejection performance of the system in the low frequency range substantially increases, when the active control is enabled, with some ripples for the out-of-plane (far right plots) force and torque.

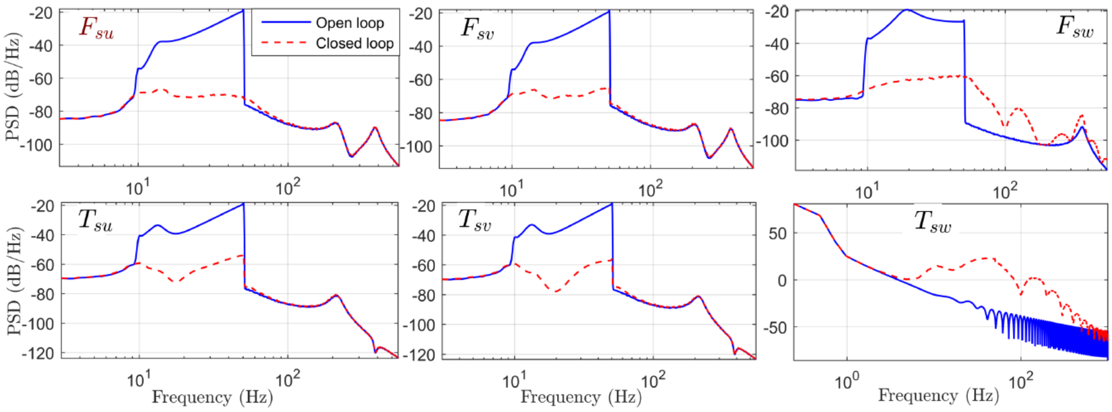

Figure 3.22: PSD of forces (top) and torques (bottom) for active-plate hybrid isolator [17].

3.2 Compensation approach

Isolators of different types can contribute to provide a quieter mechanical environment for the optical payload to operate, enabling scanning and acquisition phases. Although, continued μrad-order precision required by the beam tracking phase, to maintain the communication link between two terminals, will not be met applying these solutions only. For this reason, compensation actions by the payload are as important as spacecraft platform isolation. Usually these applications come as tip-tilt mirrors controlled by piezo-electric actuators, inserted in the optical train, called fine-steering mirrors (FSM). In this section most relevant compensation techniques for optical payloads are analysed, with a parenthesis on merging control between vibration and beam phase compensation.

Fine Steering Mirrors

FSM designs and performances have been thoroughly studied and developed to enable laser communication, interferometry and observation payloads [38, 39, 40, 41]. FSM control loops work as shown in Fig. 3.23: once the collimated beam enters the system, the FSM reflects the beam and it gets split in two, one goes in the receiving photo-diode, and the other goes in the 4-Quadrant Detector (4QD), a sensor consisting of 4 photo-diodes forming a circle, to determine the position and displacement of the beam with respect to the center. These sensors provide the feedback for the actuators of the mirror.

In [38] the Pointing Acquisition and Tracking (PAT) system for SILEX mission was developed, and its main functional scheme is shown in Fig. 3.24. The PAT is

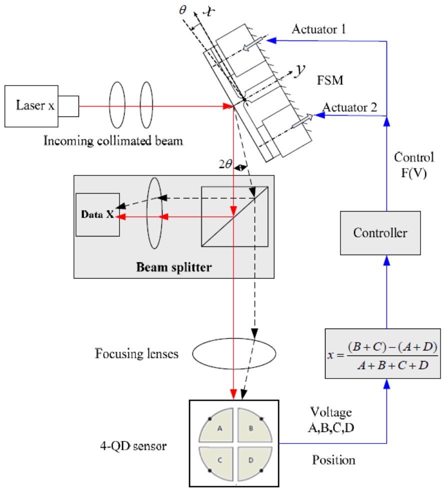

Figure 3.23: FSM control loop concept [39].

mainly composed of two stages, the Large Range Azimuth Mechanism (LRAM), providing the wide angular range for azimuth, and the FSM, performing accurate angular tuning in both azimuth and elevation. Focusing on the FSM, for the tracking phase the mirror is required to provide an angular 3σ Line Of Sight error not greater than 1.4 μrad, a really demanding performance that once again stresses out the need of a stable environment for proper operation. For this purpose a high-stiffness mechanical design was developed considering that no structural mode below 300 Hz could affect the LOS stability performances. Such stiffness should also subside the need of a launch lock device. This is more related to the translational (lateral and longitudinal) modes, while less stiff rotational modes were required, with a first rotational mode around 1.6 Hz. In the 1.6-300 Hz frequency range the FSM is expected to perform with a very tight frequency response, as described by its requirements in Fig. 3.25.

Employment of fine steering mirrors in the optical train of the payload is the reason why active micro-vibration isolation is not a common solution, as disturbances in the LOS induced by micro-vibrations in the low frequency range are "solved" modifying the beam direction.

Phase noise correction

Micro-vibrations not only affect the pointing jitter of a laser beam - they indeed can affect waves coherence and as a consequence interferometry measurements. Researchers have investigated and developed a post-correction system to counteract beam phase shifting induced by micro-vibrations [42, 43, 44, 45].

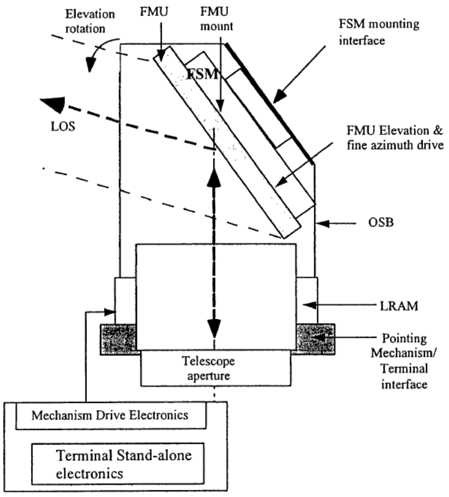

Figure 3.24: SILEX PAT schematic view [38].

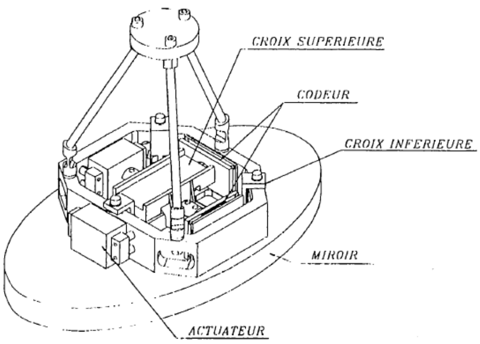

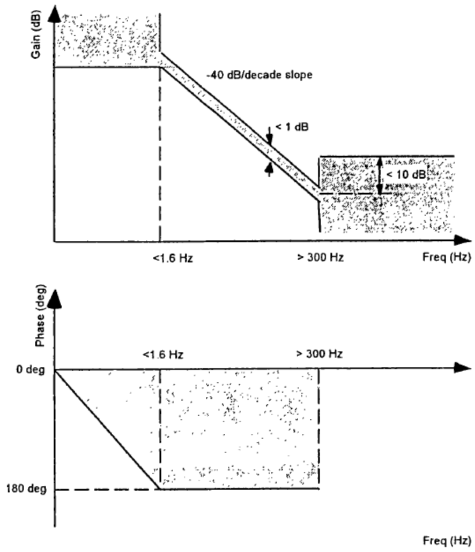

Figure 3.25: Left: SILEX FSM design. Right: Frequency response requirements for FSM [38].

These experiments were developed with the goal to reduce the phase noise induced by laser beams for an atomic interferometer. The experiment setup is shown in Fig. 3.26, and it resembles the optical bench of the original atomic interferometer. The two laser beams are generated from the same ECLD, modulated by an Acousto-Optic Modulator (AOM). The two beams are recombined at two different stations: the first recombination goes as an input to photo-diode PD1, where the beat-note between the two beams is measured and mixed with a reference 80 MHz signal to obtain the phase error signal $\varphi 1$, to be fed to the modulator driver (VCO). At the second station, the beams are split and recombined by a Michelson interferometer. One of the mirrors (ACC) is actively controlled to simulate mechanical vibrations. The recombined beam is then sent to PD2, to measure the beam phase shift ($\varphi 2$) that would be imprinted to the atomic wave phase. The post-correction is implemented measuring the vibrations of the mirror to generate a compensation signal φ_a to be added to the phase error signal $\varphi 1$.

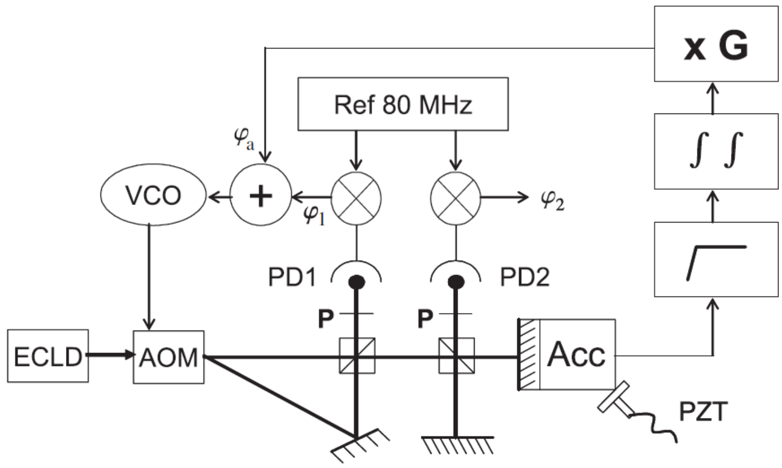

Figure 3.26: Scheme of the testbench for phase compensation [42].

Results are shown in Fig. 3.27 (left). When compensation loop is active (dashed curve), the accelerometer used to sense mirror vibrations adds his noise to the system (grey curve). This results in poor performances in the 0.1-20 Hz range, but as frequencies get higher compensation benefits are more and more evident, compared to the uncorrected phase noise (solid curve). Using a low-noise accelerometer, the feed-forward correction system was integrated in the atomic interferometer [43, 44, 45]. In Fig. 3.27 (right) the Allan Deviation of the whole system is shown, comparing performances of Classic Accelerometer (CA curve) and the developed Hybrid Gravimeter (HG curve).

Interferometry space missions requiring an extreme level of precision might consider an optical phase noise post-correction employing a similar approach, along with isolation techniques, to meet the desired goals.

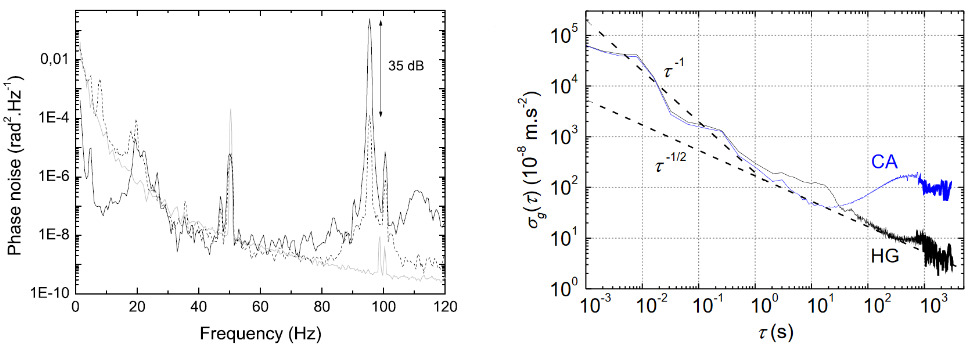

Figure 3.27: Left: rejection performances of first experiment. Right: Allan Deviation of enhanced experiment [42, 45].

Chapter 4

Micro-vibration Management

4.1 Requirements Definition

When designing an optical communication mission, it is critical to define proper pointing requirements, as performance losses due to misalignment can compromise the mission. Main pointing requirement depends on the beam waist, beam divergence angle, the transmitter power and receiver sensibility. The goal is to minimize the Bit Error Rate (BER) due to misalignment losses. This happens because laser beam has not an homogeneous power through its width, it has in fact a Gaussian shape. In fig 4.1 the scheme of a Gaussian beam is shown. The valuable "slice" of a Gaussian beam is usually defined by the limit point where its power is equal to $1/e^2$ times its peak power (which is set on the central pointing axis). This defines beam waist w_0, which describes the beam radius in $x = 0$. w_0 also defines the beam divergence, as the radius of curvature R_x is given by:

$$R(x) = x \left[1 + \left(\frac{\pi w_0^2}{\lambda x} \right)^2 \right] \tag{4.1}$$

and the Gaussian beam waist at pointing axis coordinate x is given by:

$$w(x) = w_0 \sqrt{1 + \left(\frac{\lambda x}{\pi w_0^2} \right)^2} \tag{4.2}$$

If no angular jitter is considered, given transmitter power P_t, transmitter optical loss τ_t and laser wavelength λ, the irradiance of the beam at a far-field

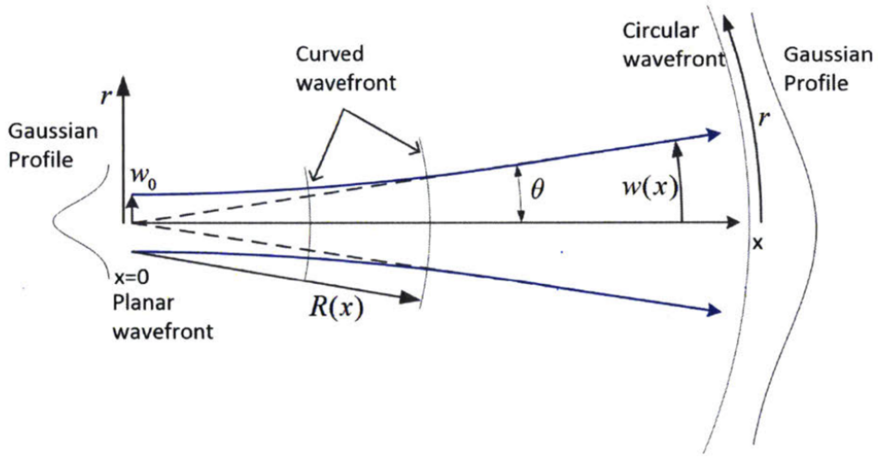

Figure 4.1: Gaussian beam scheme [46].

propagation distance R in the direction θ is defined as [47]:

$$I^0(\theta, R) = \frac{P_t \tau_t}{R2} \frac{2}{\pi w_0^2} exp\left(-2\frac{\theta^2}{w_0^2}\right), \tag{4.3}$$

whilst the received power, given receiver aperture A_r and its respective optical loss τ_r is defined as:

$$P_r = I^0(\theta, R) A_r \tau_r. \tag{4.4}$$

To obtain a valuable information at the receiver, the signal-to-noise ratio (SNR) is a critical parameter to consider. BER depends on SNR; defining SNR with Q, the BER for an intensity modulation system non-return-to-zero is given by:

$$\text{BER}(Q) = \frac{1}{2}\text{erfc}\left(\frac{Q}{\sqrt{2}}\right) \tag{4.5}$$

with erfc being the complementary error function.

Angular jitter effects on communication performance

Assuming a null bias angle, and considering a random jitter rms value σ, the pointing error can be considered as a Rayleigh distribution:

$$p_j(\theta{,}0) = \frac{\theta}{\sigma^2}\exp\left(-\frac{\theta^2}{2\sigma^2}\right), \tag{4.6}$$

which is the very same PDF described in Ch. 2, but with notation for this discussion. The PDF of the received optical intensity is defined by the beta distribution:

$$p(I) = \beta I^{\beta-1} \quad 0 \leq I \leq 1, \tag{4.7}$$

$$\bar{I} = \frac{\beta}{\beta+1}, \tag{4.8}$$

with I being the normalized intensity and $\bar{I}$ the average value. β is a parameter that puts in relationship the beam waist with the jitter rms:

$$\beta = \frac{w_0^2}{4\sigma^2} \tag{4.9}$$

Hence a new BER needs to be formulated taking in account the new PDF of the intensity [48]:

$$\begin{aligned} \overline{\mathrm{BER}}\left(Q_r\right) &= \int_0^1 p(I)\,\mathrm{BER}\left(IQ_r\frac{\beta+1}{\beta}\right)\mathrm{d}I \\ &= \frac{Q_r(\beta+1)}{2}\int_0^1 I^{\beta-1}\,\mathrm{erfc}\left(\frac{IQ_r}{\sqrt{2}}\frac{\beta+1}{\beta}\right)\mathrm{d}I, \end{aligned} \tag{4.10}$$

with Q_r being the required SNR for a desired $\overline{\mathrm{BER}}$ value, which can be chosen as a variable , so that $\overline{\mathrm{BER}}(Q_r) = a$. Once this is solved, a power penalty function L_j can be described [48]:

$$L_j = \left(\frac{Q|_{\mathrm{BER}(Q)=a}}{Q_r|_{\overline{\mathrm{BER}}(Q_r)=a}}\right) \tag{4.11}$$

In Fig. 4.2 BER behaviour related to Q_r and w_0/σ ratio (left) and the power penalty L_j related to jitter ratio, for different average BER values (right) are shown. The power penalty is not relevant for high w_0/σ ratios, but as this value becomes smaller, the penalties drastically increase.

Nevertheless, power penalty is also due to the received optical power itself. The average on-axis irradiance to the receiver considering jitter is given by [48]:

$$\begin{aligned} \langle I(0,R)\rangle &= \frac{P_t\tau_t}{R^2}\frac{2}{\pi w_0^2}\frac{\beta}{\beta+1}L_j \\ &= I^0(0,R)\tau_j L_j \end{aligned} \tag{4.12}$$

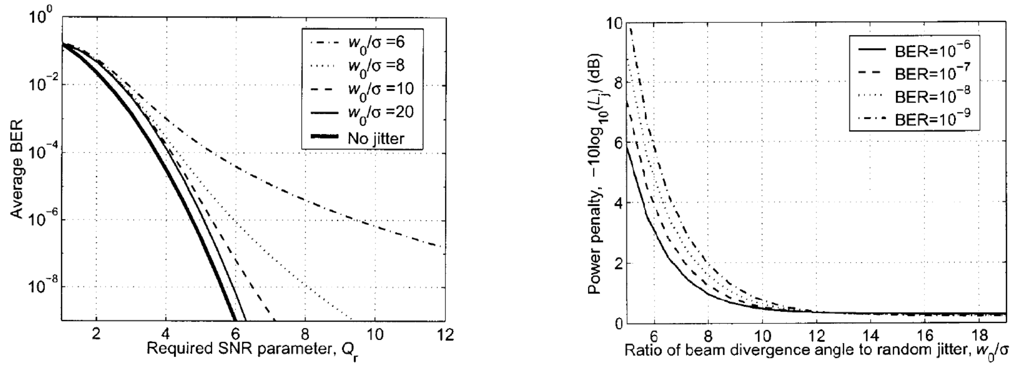

Figure 4.2: Left: relationship between average BER and required SNR Q_r, for different w_0/σ values. Right: relationship between power penalty L_j and w_0/σ, for differen average BER's [48].

with $tau_j = \beta/(\beta+1)$ defined as the average pointing loss due to angular jitter. Hence, the complete power penalty at the receiver can be written [48]:

$$\begin{aligned} L_p = & -10\log\left[\frac{\langle I(0,R)\rangle}{\langle I(0,R)\rangle|_{\mathrm{BER}=10^-6,\max}}\right] \\ \propto & -10\log P_t + 20\log R \\ & + 10\log\left(w_0^2+4\sigma^2\right) - 10\log L_j \end{aligned} \tag{4.13}$$

Thus, all losses due to transmitter power P_t, link distance R, beam divergence angle w_0, angular jitter σ and power penalty linked to BER L_j are considered. The equation is numerically solved, in order to obtain a minimum w_0/σ value for the desired $\overline{\mathrm{BER}}$. In Fig. 4.3 (left) the numerical solution of the power penalty is shown for different BER values, and the minimum of each curve corresponds to the optimal w_0/σ value. Also, analytical fit of the optimal w_0/σ with respect to desired average BER (right) is shown.

It is also noteworthy that different modulation schemes, influencing of course BER and SNR, can handle different magnitudes of vibrations [14].
Setting some system parameters regarding the optical communication scheme would allow to have a first estimation about the vibration level that can be handled without significant performance losses.

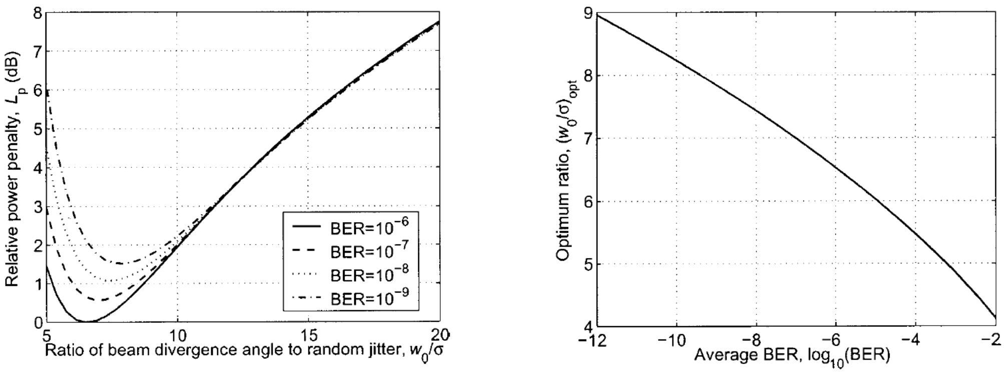

Figure 4.3: Left: Numerical plots for power penalty, to define optimal w_0/σ. Right: interpolation of optimal w_0/σ given the average BER values.[48].

4.2 Source modelling and Micro-vibration Budget

Using a model based approach, it is possible to assess an expected magnitude of micro-vibrations. ECSS [12] provides some guidelines about the micro-vibration analysis flow. This is divided in three main steps:

1. Determination of the structural transfer functions between the disturbance location and the receiver one, usually derived from a finite element model (FEM) analysis of the spacecraft in its on-orbit configuration, including, in a variable level of detail, disturbance sources and payloads integrated models.
2. Application of the disturbance source forcing functions.
3. Evaluation of response at the receiver (usually the payload) locations.

The analysis is usually developed in the frequency domain. The result of such an analysis will give the jitter of the payload LOS. For step 1 a modal analysis should be performed, using FEM-based softwares like Nastran or Ansys, to derive the transfer functions in the frequency range of interest.
As for point 2 and 3 of the analysis, these are usually performed using MATLAB models which resemble the source disturbances, and combined with the transfer functions from point 1 will determine the response at the payload.

As previously discussed, micro-vibrations are characterized by a wide frequency range. FEM analysis is a valid analysis instrument for low frequency, but as

frequencies increase FEM results are less and less reliable. For this reason, when studying a micro-vibrations problem, FEM results are limited to the low frequency region, as for mid and high frequency ranges a different method is used: the Statistical Energy Analysis (SEA).
SEA already proved to be a useful tool in micro-vibration analysis [12, 49]. SEA basic model consists of two linear, weakly coupled oscillators exchanging energy when excite by uncorrelated random forces . The critical variables of this analysis are the total energy stored in the local modes of the respective sub-domains.

The vibrational energy E is defined as the sum of potential and kinetic energies integrated in the related frequency band, while power P is the mean rate of change of energy in time domain between the two oscillators. When in steady-state conditions, a set of two oscillators exchange a power proportional to their energy difference:

$$\frac{P_{12}}{\omega} = B\left(\omega_1, \omega_2\right)\left[E_1 - E_2\right] \tag{4.14}$$

B is a coefficient depending on system parameters, such mass, damping factor, coupling stiffness and uncoupled eigenfrequencies ω_1 and ω_2. P_{12} reaches a maximum when ω_1 and ω_2 coincide, whilst there is a drastic reduction when the two eigenfrequencies are different.
Considering a frequency band $\Delta\omega$ with a central frequency ω_c, Eq. 4.14 can be extended to the coupling of continuous subsystems, assuming that their energy is proportional to the local modal density n, or their mode number N:

$$N = n\frac{\Delta\omega}{2\pi}\omega \tag{4.15}$$

SEA theory assumes that modes are uniformly distributed over $\Delta\omega$, so that the description about the modes is limited to how many resonating modes (N)are present in $\Delta\omega$. Doing this, Eq. 4.14 becomes:

$$\frac{P_{12}}{\omega} = N_1 N_2 \langle B\rangle_{\Delta\omega}\left[\varepsilon_1 - \varepsilon_2\right] \tag{4.16}$$

In this case the modal data set is considering local modes of subsystems 1 and 2 only, resonating in the same frequency band. Subsystem 1 ith mode is paired to subsystem 2 ith mode, so that $N_1 N_2$ modes exchange energies through a mean modal B coefficient, with each mode carrying a modal energy ε.

Power balance for each subsystem can be determined considering power input from applied sources, internal dissipation and power coupling:

$$\begin{aligned}\left\{\begin{array}{c}P_1\\P_2\end{array}\right\} &= \left[\begin{array}{c}\eta_1\omega N_1\varepsilon_1 + N_1N_2\omega\langle B\rangle\,[\varepsilon_1-\varepsilon_2]\\ N_1N_2\omega\langle B\rangle\,[\varepsilon_2-\varepsilon_1]+\eta_2\omega N_2\varepsilon_2\end{array}\right]\\ &=\omega\left[\begin{array}{cc}\eta_1N_1+N_1N_2\langle B\rangle & -N_1N_2\langle B\rangle\\ -N_1N_2\langle B\rangle & \eta_2N_2+N_1N_2\langle B\rangle\end{array}\right]\left\{\begin{array}{c}\varepsilon_1\\\varepsilon_2\end{array}\right\}\end{aligned} \tag{4.17}$$

and in a compact way, defining $[L]$ the loss matrix:

$$\left\{\begin{array}{c}P_1\\P_2\end{array}\right\} = \omega[L]\{\varepsilon\}, \tag{4.18}$$

defining η_1, η_2 the the damping loss factors.
Coefficient B cannot be derived from the coupled equation of motion as the "weak coupling" assumption itself renders the coupling conditions unknown. It is instead derived from wave theory, considering a wave transmission problem through a junction with a given incidence. As the frequencies become higher, interacting modes can be in large number. Thus, the incidence is assumed to be random and B is computed as proportional to the diffused field wave transmission coefficient.
Doing so modal energies ε can be simply calculated through inversion of the loss matrix $[L]$. Defining the coupling loss factor as $\eta_{12} = N_2\langle B\rangle$, power exchange can be defined as:

$$\frac{P_{12}}{\omega} = N_1\eta_{12}\varepsilon_1 - N_2\eta_{11}\varepsilon_2 = \eta_{12}E_1 - \eta_{11}E_2 \tag{4.19}$$

with $E = m\langle v^2\rangle$ the total energy stored by subsystems, with total mass m and mean space-frequency averaged velocity $\langle v^2\rangle$.

A SEA model set up in this way returns a good prediction about micro-vibrations statistic behaviour in the mid and high frequency ranges. Although, this method is not suitable for low frequency range, where FEM analysis still remains the way to go.
The SEA model analysed is simplest one, with two subsystems only. Obviously this system can be scaled up to represent as many subsystems as needed. In Fig. 4.4 for example, the SEA model used for the OLYMPUS mission is shown.

4.2.1 Source modelling

Both FEM and SEA models require forcing functions to accurately represent the structural response to disturbances. These forcing functions are derived from

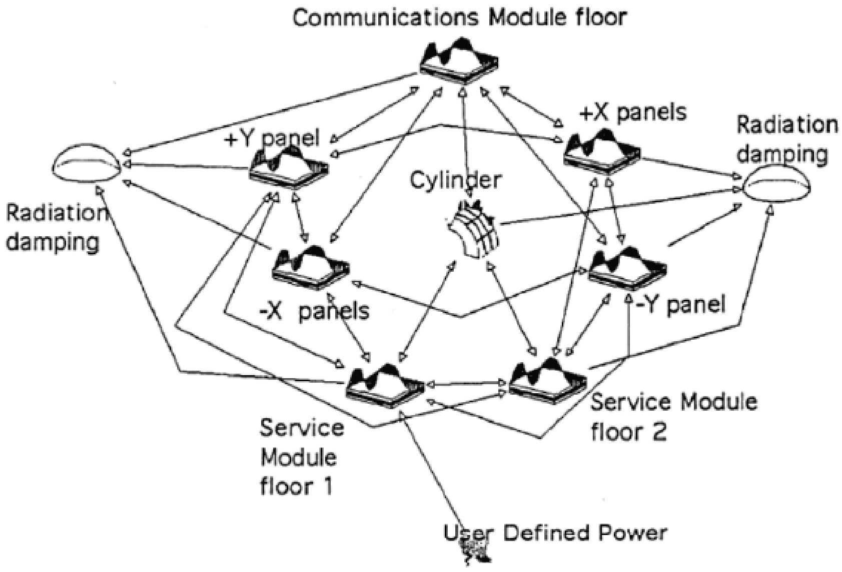

Figure 4.4: OLYMPUS SEA model [49].

disturbance sources, which have been already discussed in Ch. 3. It becomes critical then to provide accurate source models that describe the vibrational behaviour.

Reaction wheel modelling

Reaction (and momentum) wheels represent the most critical disturbance source for common spacecrafts, hence capturing their vibrational characteristics properly is critical for a mission involving sensitive payloads. Given the criticality, RWA models have been thoroughly investigated and proposed [18, 19].
Disturbances of a reaction wheel can be separated in three main categories:

1. Wheel mass imbalances (static and dynamic imbalance)
2. ball bearing imperfections
3. electric motor ripples

Among the three, disturbances generated by mass imbalances are considered the most relevant, but it is the interaction between these components to generate the ultimate disturbance for this device.

In Fig. 4.5 conceptual schemes of static and dynamic imbalances are shown. Static imbalance U_s is the distance of the wheel centre of gravity from its rotation axis. This is represented by a small mass m placed at a distance r from the rotation axis. This generates a sinusoidal radial force F_s:

$$F_s = m \cdot r \cdot \omega_w^2 = U_s \cdot \omega_w^2 \tag{4.20}$$

$$U_s = m \cdot r \tag{4.21}$$

Dynamic imbalance U_d is the cross product inertia of the flywheel, due to the misalignment between the wheel principal inertia axis and the rotation axis. When modelled, this is represented by two diametrically opposed masses at a distance r from the rotation axis, placed at an axial distance d from each other. The result is a torque T_d, with the vector perpendicular to the rotation axis. For this reason, this disturbance is also called "rocking".

$$T_d = m \cdot r \cdot d \cdot \omega_w^2 = U_d \cdot \omega_w^2 \tag{4.22}$$

$$U_d = m \cdot r \cdot d \tag{4.23}$$

Typical values for static and dynamic imbalance for reaction wheels are $U_s = 5$ gcm and $U_d = 20$ gcm^2 [12].

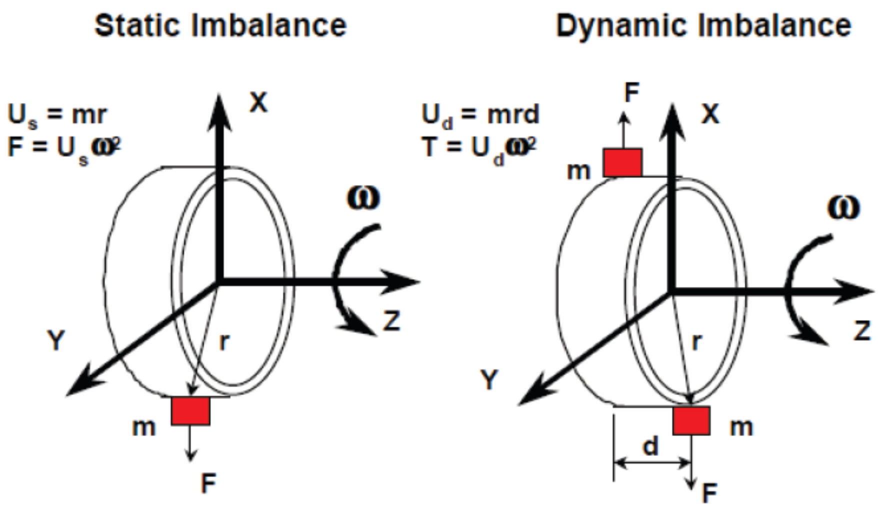

Figure 4.5: Reaction wheel mass imbalances [12].

Ball bearing disturbances are caused by mechanical imperfections of the bearings themselves, whether it is due to the rolling element, the cage or the raceways. These disturbances are a series of harmonics, multiples of the relative rotation rates between the different moving parts in the bearing. Part of these disturbances could be overcome re-designing the wheel with magnetic bearings [50], but this would add complexity to the system for not so critical benefits.

As for motor imperfections, usually brushless DC motors drive the wheel. This motor can generate disturbances from torque ripple, motor cogging and motor driver anomalies, with the latter being less relevant.
Torque ripple is the change in the motor torque with respect to the angular position, which is represented by a series of harmonics with an amplitude proportional to the motor current. As for its magnitude, considering a perfectly aligned motor the ripple torque is generally 14.3% of the nominal motor torque. Rippling models are usually derived from Fourier Transformation of the torque waveform to identify the ripple tipical frequencies.
Motor cogging generates from magnetic disturbances between the stator and the rotor of the brushless motor, resulting in a noise torque.

Modelling of the wheel support is critical as well, as it determines how such disturbances will be transmitted to the main structure [51]. In Fig. 4.6 a simple schematics of the RWA support is described, along with fundamental resonance modes visualization. These modes are:

1. Axial translation mode: $f_a = \sqrt{\frac{k_a}{m}}$
2. Radial translation mode: $f_r = \sqrt{\frac{k_r}{m}}$
3. Radial rocking mode: $f_o = \sqrt{\frac{K_T}{I_{xx}}}$

with m the mass of the supported wheel, k_a the support stiffness in the axial direction, k_r the support stiffness in the radial direction, K_T the cross-axis torsional stiffness and I_{xx} the cross-axis moment of inertia of supported wheel. Support models could also be more elaborate, in order to simulate and test isolating supports.

In rotordynamics it is common to observe a whirl mode as the spinning rate increases: this is effect of the gyroscopic precession affecting the rocking mode. The whirl can be split into a counter-rotating whirl, characterised by a slow natural frequency, and a whirl in the same direction of the spinning wheel, with a higher natural frequency. These frequencies diverge as spinning rate increases:

$$f_n(\omega) = \pm\frac{I_{zz}\omega}{2I_{xx}} \pm \sqrt{\left(\frac{I_{zz}\omega}{2I_{xx}}\right)^2 + \frac{K_t}{I_{xx}}} \tag{4.24}$$

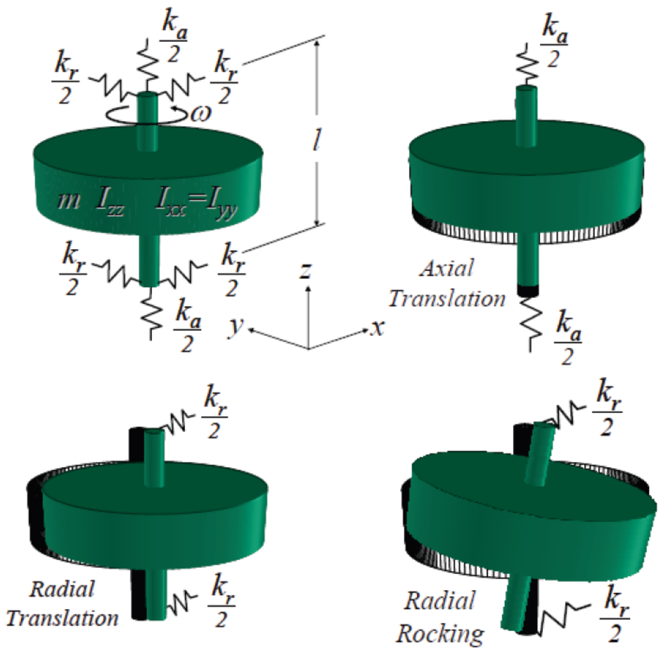

Figure 4.6: Reaction wheel simplified support model [51].

with ω the wheel spinning rate.

Results from frequency analysis on rotating mechanisms are commonly plotted on Campbell diagrams. In Fig. 4.7 (left) principal modes of the wheel and frequencies of the discussed disturbances are shown in a Campbell plot. Black curves describe fundamental modes of the RWA, and disturbance frequencies with respect to the spinning rate have been added. Waterfall plots (right) show radial and axial force and moments induced by the modes and the imperfections. It can be seen how magnitude of the disturbances mostly increase linearly with the spinning rate. Although, when the disturbance curves cross a fundamental mode, a resonance might occur, resulting in critical peaks. Resonances between disturbance frequency, fundamental mode of the RWA and fundamental mode of the main spacecraft structure might result in severe micro-vibrations.

Solar array and antenna mechanisms modelling

Solar array and Antenna drive mechanisms generally employ stepper motors. The disturbance of the motors themselves, along with the structural response of the appendages, induce disturbance to the main structure. Stepper motors are characterized by gears and bearings imperfections, which, as seen previously in the RWA case, can result in a wide frequency spectrum of micro-vibrations. In

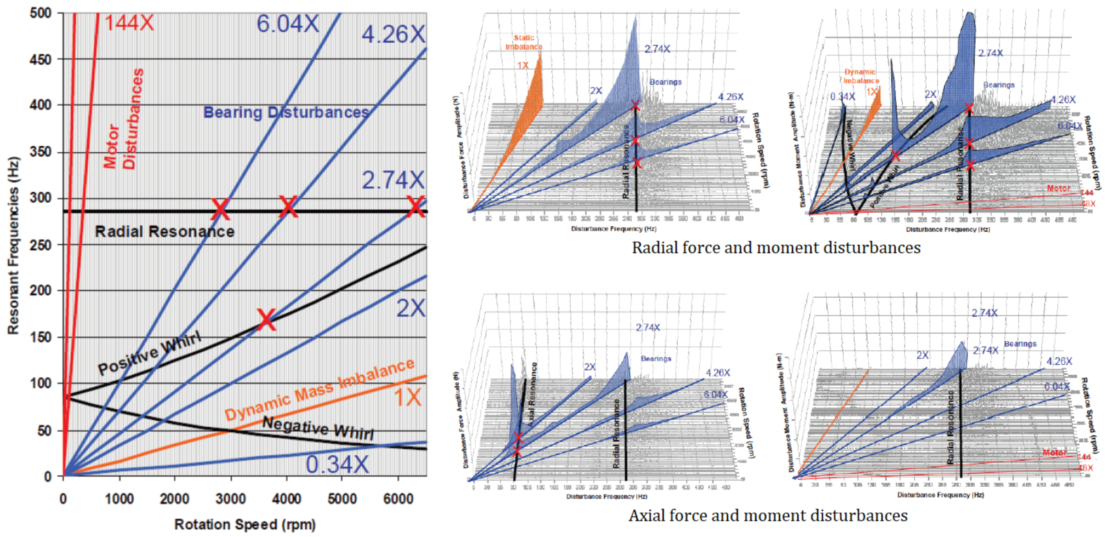

Figure 4.7: Left: Campbell plots with main resonance modes of the wheel and disturbance plots. Right: Waterfall plots [51].

this case, a FEM model is required to accurately reproduce the appendage-main structure response. A complete model is shown in Fig. 4.8, where the FEM takes in input the driver torque (MGU torque) to return the angular displacement in the line of sight.

4.2.2 Micro-vibration budget

Ideally, the micro-vibration analysis would be performed on the whole satellite, involving both payload and platform models. Although, the two modules are usually competence of two distinct entities, hence the analyses will be performed on a module level. For this reason, defining the payload interface requirements is critical for a good micro-vibration budget. An example for the allocation of such budget for a wide frequency range is derived in [15]. The main idea relies on separating the frequency range of interest in smaller bands, with the goal to characterise each of these with a specific peak, belonging for instance to a RWA fundamental mode or a structural bending mode. Once the accelerations at the payload interface are measured, each band will be characterised by an average, flat acceleration a_{avg} through the whole band, exception made for the central frequency of the band, where the peak acceleration a_{pk} is placed. Average acceleration a_{avg} is computed excluding a_{pk}. Once this platform analysis is performed, the payload developer can evaluate the requirement with a sine-sweep signal with the magnitude of a_{peak}.

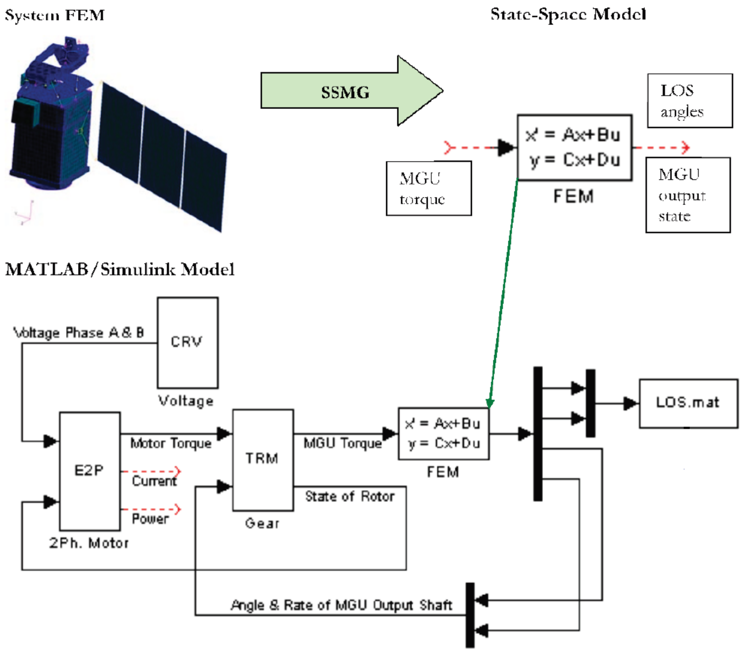

Figure 4.8: SADM model logic [49].

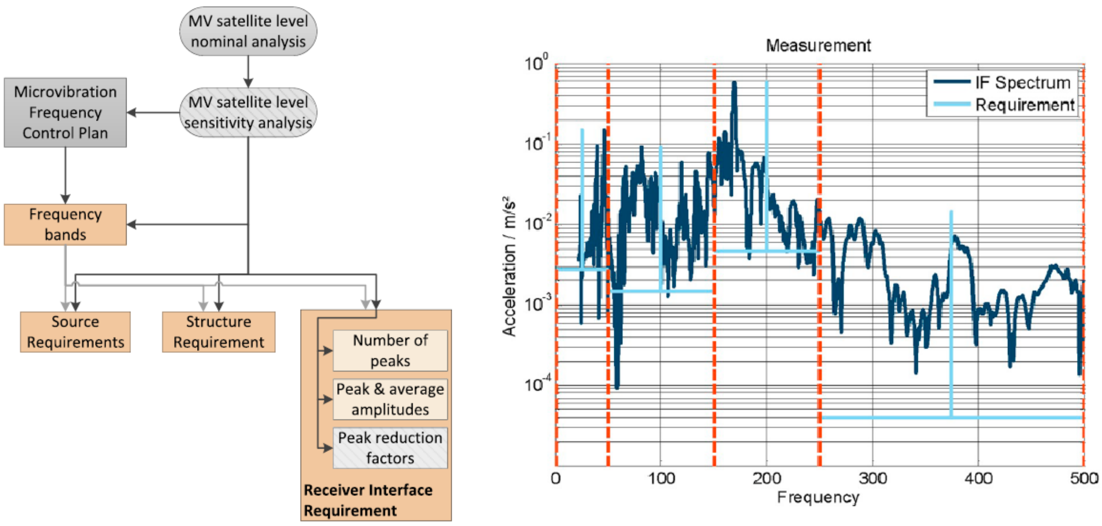

Figure 4.9: Left: payload-platform interface requirement logic. Right: Micro-vibration budget allocation [15].

This allows to define the worst case scenario in each frequency band, and determine the impact on the payload LOS. Although, it is noted how this worst case scenario does not take in account the structural coupling between the platform and the payload. In the coupling scenario, most likely the peak will be split in multiple resonances with reduced amplitude. A reduction factor c_{red} due to coupling effects was derived from experience [15]:

$$c_{red} = \frac{\max\left(\varphi_{LoS,\ \text{coupled}}\left(f\right)\right)}{\max\left(a_{pk} \cdot H_{PL}\right)}. \tag{4.25}$$

This reduction factor is defined as the ratio between maximum LOS error in the coupled configuration $\varphi_{LoS,\ \text{coupled}}$ and the payload interface peak accelerations a_{pk} multiplied by the payload frequency response H_{PL}. This frequency band method has proven to be a good reference for interface disturbance.

This method can provide a good systematic approach in order to identify critical disturbance frequencies in the interface, and iterate until the requirements are met. In this case, iteration means to address such disturbances, and perform their minimisation.

4.3 Disturbance minimisation

The most common approaches for disturbance minimisation, such as isolation and compensation, have been widely discussed in Ch. 3. The goal of this section is in fact to investigate how disturbances can be addressed on a higher level, satellite-wise. To address the minimisation problem there is not a univocal solution, and different ways can lead to a equally viable mission.
For instance EDRS satellites, whilst sharing the same optical payload (Tesat LCT), same orbit characteristics, and same mission (LEO-to-GEO optical data relay), apply two different approaches to minimise the disturbances induced by the satellite platform and provide the quiet mechanical environment required for the operation the payload.
EDRS-A satellite employs the PEMS isolator, already discussed in Ch. 3, to address platform disturbances [8]. This is a very aggressive platform-to-payload solution. Even though it does not reach the complexity of active isolation, it nevertheless required the design and testing of a new mounting system, also increasing mass and size of the satellite.
EDRS-C satellite opted for addressing directly the source instead [9]. Reaction wheels, deemed the most critical disturbance for the mission, have been placed as far as possible from the main central structure, in order to avoid a direct mechanical transmission of the vibrations and disperse as much energy as possible through a longer load path. In addition to this, RWA have also been passively isolated from the rest of the platform. This source-to-platform approach, though being more discrete, proved equally effective for the mission, and the payload is now flying fully operational.

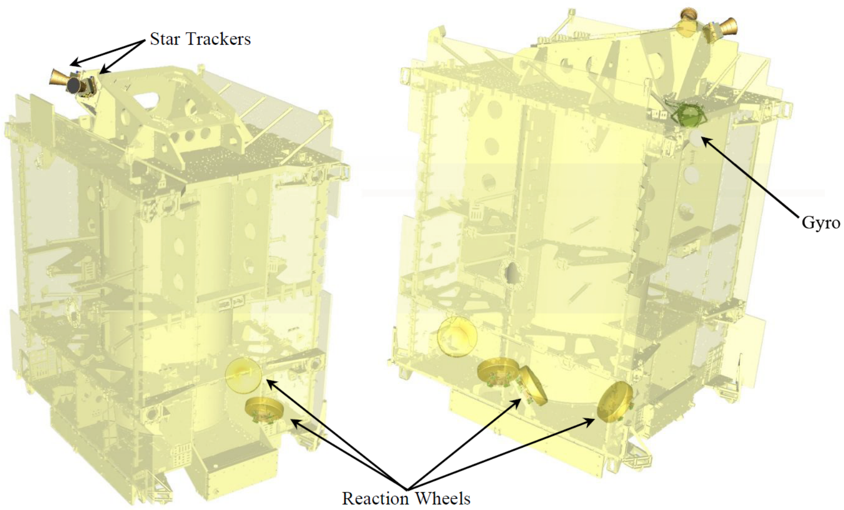

Figure 4.10: EDRS-C RWA accommodation on board of the platform [9].

The approach used for the EDRS-C satellite is an example of how careful source accommodation could allow to a less demanding isolation system. Although, it is not always possible to demand important platform modifications for the payload developer. These are the cases in which EDRS-A-like solutions can be considered.

It is also critical to investigate mission operations and their impact on the LOS. While operating, satellite orbital parameters are subject to perturbation, mostly due to Earth gravity gradients and luni-solar disturbances [52]. For a GEO orbit, where relative position with respect to certain terrestrial location needs to be maintained in a tight spatial and temporal frame, frequent Station Keeping (SK) manoeuvres are required. SK manoeuvres employ on-board chemical thrusters to correct the orbit. These firings induce a high level of micro-vibration, which are hard to overcome for most payloads. For this reason, usually optical communication are turned off and put in a "park position", in order to protect the external optics from thruster plumes [9, 53]. While this is the common ground for current FSO communication missions, this would not be acceptable any longer in a prospective mission maintaining optical link for 24 hours a day.

Electric thrusters reached a technology level where they can be envisioned to perform critical SK manoeuvres, and all-electric satellite platforms too. Basic concept of electric propulsion is the acceleration of propellant particles by generating an electric (more common) or an electro-magnetic field. Advantages for employing these thrusters would come from their reduced magnitude of thrust,

that would induce a lesser amount of vibration to the structure. This is also due to a simpler mechanical design of the thrusters. Another advantage, on a system level, is the lighter propulsion group, allowing to allocate more mass for the payload. Operational concept of electric thrust envisions continuous firing, in opposition with the impulsive manoeuvres of the chemical thrusters. Introducing a vibration source for a prolonged time, but with manageable magnitude, could enable the continuous operation of the optical communication payload.
A drawback of employing electric propulsion is the additional power requirement for the thruster activation. For instance, OHB Electra platform is able to provide 10 kW of power to the payload, but during the operation of the electric thrusters the payload power decreases down to 3.5 kW, in order not to overload the electric subsystem [54].

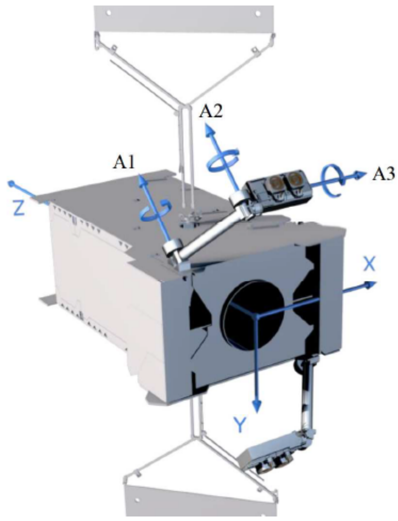

Figure 4.11: OHB Electra platform [54].

Another critical operation is the desaturation of the reaction wheels. As RWA counteract the disturbance torques induced by space environment, they store a momentum bias and increase their speed. Although, wheels are characterised by a spinning rate limit, and when they reach it they are no longer able to counteract disturbance torques. When this happens the wheel is defined saturated [55]. At this point, momentum dumping is required, but if the wheel decreased its speed without any counteracting torque, the satellite would be induced to spin in the opposite direction, and the attitude control would be compromised. To avoid this, momentum dumping is performed activating some other device on board to create a counteracting torque during this operation. Where the magnetic field is strong enough (i.e. in LEO orbits), magnetorquers can be used to enable momentum dumping. When this is not possible, as in GEO orbits, thrusters are generally employed for this operation. This is because thrust direction seldom coincide with centre of gravity of the satellite, thus a torque is induced. When this is performed with chemical thrusters, short firings would imply a rapid decrease in the spinning rate of the wheel is envisioned, inducing additional degradation to the payload LOS. If electrical propulsion is employed, this dumping is more gradual, hence controlled by any means, as for wheel spinning rate and overall satellite disturbances.

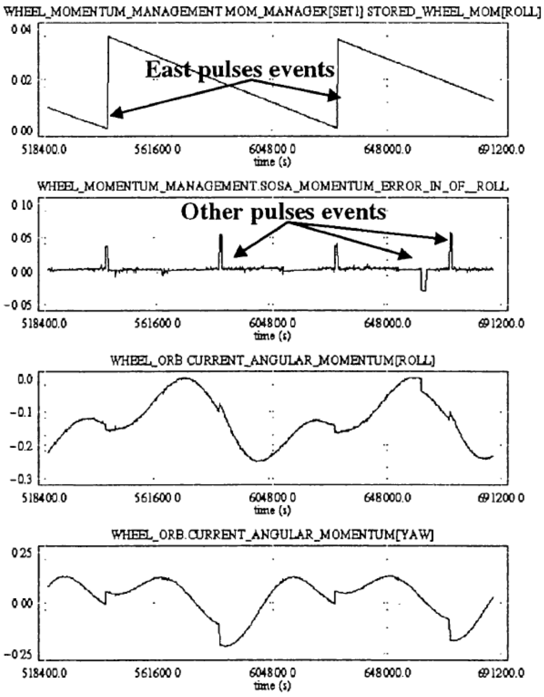

Figure 4.12: Wheel momentum management with respect to SK manoeuvres (pulses) [56].

A drastic design change could envision the removal of the reaction wheels for payloads requiring ultra-stable platform. This is the case of ESA's Gaia and LISA Pathfinder missions [57]. Gaia is a deep space observatory designed to map the Milky Way, while LISA is a technology demonstration mission leading the way for a gravitational observatory in space, using interferometry. Both missions involve highly susceptible instruments, where the level of micro-vibrations needs to be put down to the minimum. For this reason, instead of employing reaction wheels, these missions used micro-thrusters to address the attitude and orbit control. These cold gas thrusters have a thrust range from 1 μN up to 1 mN, with a thrust control resolution of 0.1 μN. Hence, such a fine thrust control enables accurate pointing without the disturbances induced by rotating mechanisms. Although, it is important to note the orbit nature of these missions: both spacecrafts orbit around Sun-Earth Lagrangian points (Gaia around L2, LISA around L1), and their missions do not foresee a high dynamic range for attitude control, due to a quieter (yet, of course, unstable) environment in terms of external disturbances.

Considering an Earth-orbiting mission, micro-thrusters with a greater thrust capability would be required, as for GEO-Ground pointing, and even more for GEO-LEO pointing, fast and precise slew capabilities of the ADCS are required. Also, for space platforms characterised by a mass in the order of thousands of kilograms, thruster-based ADCS would require massive propellant tanks, an aspect that greatly reduce the appeal of this approach for such missions.
Nevertheless, appeal still holds for miniaturized platforms, like pico- and nano-satellites (e.g. Cubesats) [58].

4.4 Requirements verification

When a first physical realization of the spacecraft platform and/or the payload is achieved, micro-vibration tests on the real model can be performed. The ideal setup would involve the representative satellite, with platform and payload integrated together. Although, modular tests, i.e. platform-only or payload only, may be considered for a number of reasons. For instance, if an isolation device was designed for the payload, a verification test involving the payload and the isolator would be needed in order to assess the rejection performances [8]. On the other hand, platform-only tests could be envisioned, using a dummy payload, in order to investigate criticalities such as eventual resonance modes between disturbance sources and the structure [59].
Such tests have several objectives: first of all, verification of structural behaviour of the physical model in the space-deployed configuration. Also, data retrieved from testing can be then compared with the expected values obtained from the mathematical model, in order to validate or update the analysis for future works. Depending on the payload, measurements from accelerometers can give an indication whether the sensed micro-vibration level is acceptable or not. Specifically for optical payloads, a fully integrated satellite can serve as verification for LOS pointing degradation.

Test setup for micro-vibration verification is logistically complex. Replying on-orbit floating conditions is not a trivial task; also, presence of air induce acoustic effects. In order to get closer to a free-fall condition, usually test setups

employ a suspension system, composed by flexible straps.
The suspension system also brings the advantage of isolating the spacecraft model from mechanical background noise, which for sensitive measurements, such as the case of micro-vibrations, can induce critical errors. Background noise magnitude should be assessed before the test, in order to understand if this interference could heavily affect measurements quality.

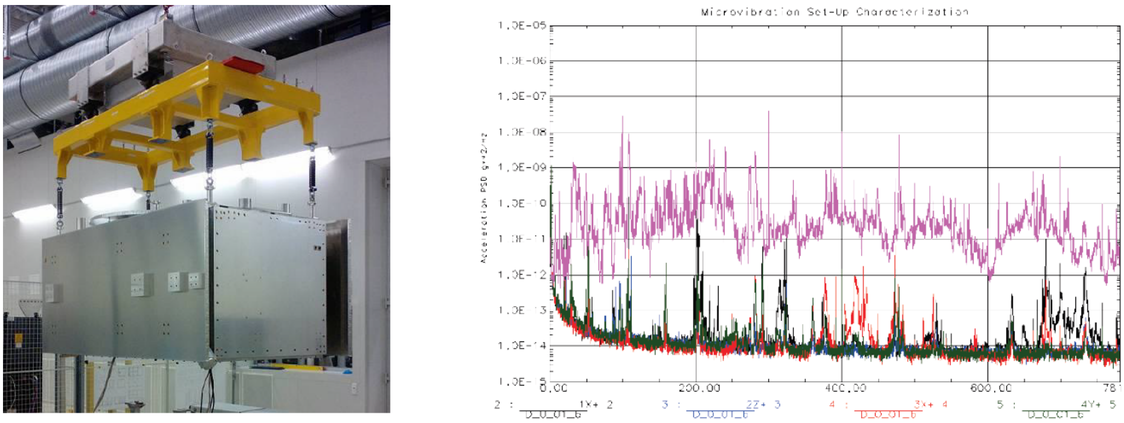

Figure 4.13: Left: Typical suspension system [59]. Right: suspension system response (magenta curve) and spacecraft accelerometers (darker curves). Suspension system manages to isolate the sensitive accelerometers from critical background noise [60].

Typical tests include sinusoidal disturbance signal, to investigate structural modes, and random noise vibrations in a wide frequency range [12].
More detailed analysis can be performed, to address specific disturbance sources. For instance, effects of reaction wheels, simulating nominal and off-nominal on orbit operations can be investigated [59].

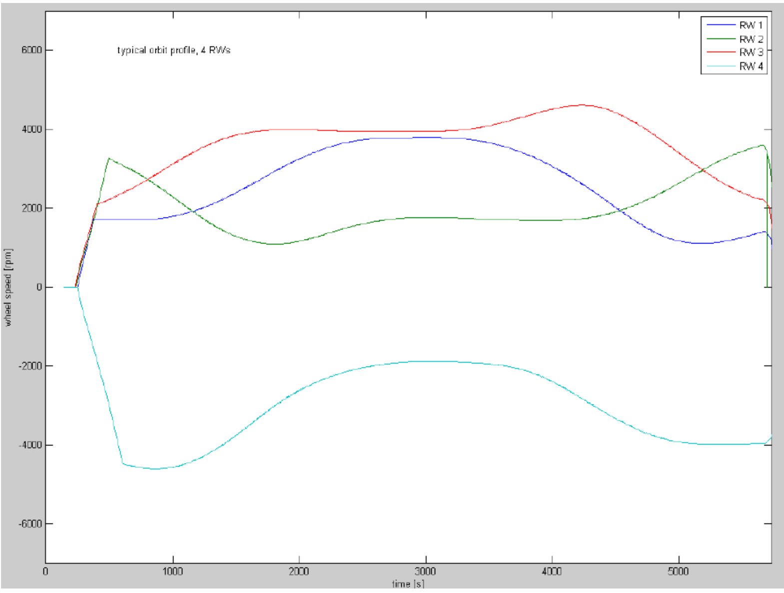

Figure 4.14: Nominal on-orbit wheel operation, activated during micro-vibration test [59].

Conclusions

The thesis carried out an analysis on micro-vibrations aspects that could affect the boresight jitter of FSO Communication payloads, in the context of a supporting activity for upcoming Kepler navigation constellation at the Institute for Communication and Navigation of the German Aerospace Center.
Statistical elements useful for the stochastic process have been explicited, and most relevant missions for on-board micro-vibration measurements investigated. An experiment to study the effect of the angular jitter was developed and conducted between two optical terminals developed by DLR engineers in the near-field range. Future works for the experiment involve the acquisition of the signal at the receiver terminal, optimisation of the signal for looping purposes, and a far-field test.
Critical disturbance sources such as Reaction Wheel Assemblies, Solar Array Driver motors and thrusters, have been identified through literature review, and their possible damping and compensation have been investigated. Solutions for mechanical isolators between the source and the satellite platform or between the platform and the payload interface. Fine-steering mirrors implemented in the optical payload can also function to compensate low frequency jitter. From the experience of real missions, the most common combination appears to be the employment of passive mechanical isolators, either in the source-platform or platform-payload configuration, along with FSM mounted on board of the payload. Passive isolators would damp the high-frequency wider range of micro-vibrations, while FSM would address the low-frequency range. Furthermore, a "post-processing" approach, that manages to compensate the coherent source phase-shift induced by vibration. This could be of interest for space-based laser interferometry.
A system-level analysis on micro-vibration budget was conducted. Relation between payload characteristics and acceptable vibration magnitude was discussed. This magnitude would be then compared with vibration simulations of the spacecraft and its related disturbance sources. While classic FEM modal analysis is not a reliable instrument for high frequency micro-vibrations, Statistical Energy Analysis (SEA) proved to provide a good measurement of the phenomenon. Once

a first estimation of the expected micro-vibrations is given, it was discussed how it is possible to perform the disturbance minimisation, empolying the instruments developed in the former chapters, and finally how to verify that the requirements for the sensitive payload can be verified, through tests performed with a suspension system.

Bibliography

[1] Christoph Günther. "Kepler - Satellite Navigation without Clocks and Ground Infrastructure". In: (2018).

[2] Hemani Kaushal and Georges Kaddoum. "Optical Communication in Space: Challenges and Mitigation Techniques". In: *IEEE Communications Surveys & Tutorials* 19.1 (2017), pp. 57–96. DOI: 10.1109/comst.2016.2603518.

[3] Jurgen Franz. *Optical communications : components and systems : analysis, design, optimization, application*. New Delhi: Narosa Publ House, II, 2000. ISBN: 9788173191459.

[4] Arun K. Majumdar and Jennifer C. Ricklin. *Free-Space Laser Communications*. Springer New York, Nov. 26, 2007. 432 pp. ISBN: 0387286527. URL: https://www.ebook.de/de/product/6413412/free_space_laser_communications.html.

[5] Morio Toyoshima. "Trends in satellite communications and the role of optical free-space communications [Invited]". In: *Journal of Optical Networking* 4.6 (2005), p. 300. DOI: 10.1364/jon.4.000300.

[6] A. Dickinson, G. Oppenhäuser, and J. Sandberg. "The Artemis Program". In: *ESA Bulletin, No. 91, August 1997, pp. 32-39* (1997).

[7] Takashi Jono et al. "In-orbit Experiment Result of Inter-satellite Laser Communication by OICETS (Kirari)". In: (2007).

[8] D. Poncet, S. Glynn, and F. Heine. "Hosting the first EDRS payload". In: *International Conference on Space Optics — ICSO 2014*. Ed. by Bruno Cugny, Zoran Sodnik, and Nikos Karafolas. SPIE, 2017. DOI: 10.1117/12.2304091.

[9] R Migliore et al. "Outlook on EDRS-C". In: *International Conference on Space Optics — ICSO 2016*. Ed. by Nikos Karafolas, Bruno Cugny, and Zoran Sodnik. SPIE, 2017. DOI: 10.1117/12.2296160.

[10] Frank Flechtner et al. "What Can be Expected from the GRACE-FO Laser Ranging Interferometer for Earth Science Applications?" In: *Surveys in Geophysics* 37.2 (2015), pp. 453–470. DOI: 10.1007/s10712-015-9338-y.

[11] *ESA Pointing Error Engineering Handbook ESSB-HB-E-003*.

[12] *Spacecraft mechanical loads analysis handbook, ECSS-E-HB-32-26A*.

[13] Cornelius Dennehy and Oscar S. Alvarez-Salazar. *Spacecraft Micro-vibration: a survey*. Tech. rep. NASA Langley Research Center, 2018.

[14] Shlomi Arnon, Stanley R. Rotman, and Norman S. Kopeika. "Performance limitations of free-space optical communication satellite networks due to vibrations: direct-detection digital mode". In: (1997). Ed. by Itzhak Shladov and Stanley R. Rotman. DOI: 10.1117/12.281392.

[15] Frank Steier et al. "Managing the microvibration impact on satellite performances". In: *Acta Astronautica* 162 (2019), pp. 461–468. DOI: 10.1016/j.actaastro.2019.06.027.

[16] Morio Toyoshima et al. "In-orbit measurements of spacecraft microvibrations for satellite laser communication links". In: *Optical Engineering* (2010).

[17] Valentine Preda. "Robust Microvibration Control and Worst-case Analysis for High Pointing Stability Space Missions". PhD thesis. University of Bordeaux, 2017.

[18] Rebecca A. Masterson. "Development and validation of empirical and analytical reaction wheel disturbance models". MA thesis. Massachussetts Institute of Technology, 1999.

[19] Daniele Addari. "A semi-empirical approach for the modelling and analysis of microvibration sources on-board spacecraft". PhD thesis. University of Surrey, 2016.

[20] Manfred E. Wittig et al. "In-orbit measurements of microaccelerations of communication satellite Olympus". In: *Free-Space Laser Communication Technologies II*. Ed. by David L. Begley and Bernard D. Seery. SPIE, 1990. DOI: 10.1117/12.18234.

[21] Juraj Poliak et al. "Laboratory Demonstrator of Optical Inter-satellite Links for the Kepler System". In: *Proceedings of the 31st International Technical Meeting of The Satellite Division of the Institute of Navigation (ION GNSS 2018)*. Institute of Navigation, 2018. DOI: 10.33012/2018.15886.

[22] Janis Surof et al. "Laboratory Characterization of Optical Inter-satellite Links for Future GNSS". In: *Proceedings of the 32nd International Technical Meeting of the Satellite Division of The Institute of Navigation (ION GNSS 2019)*. Institute of Navigation, 2019. DOI: 10.33012/2019.17042.

[23] P. L. Davis, J. F. Wilson, and R. E. Jewell. "Hubble space telescope reaction wheel assembly vibration isolation system". In: *Damping 1986 Proceedings* (1986).

[24] D. Kamesh, R. Pandiyan, and Ashitava Ghosal. "Passive vibration isolation of reaction wheel disturbances using a low frequency flexible space platform". In: *Journal of Sound and Vibration* 331.6 (Mar. 2012), pp. 1310–1330. DOI: 10.1016/j.jsv.2011.10.033.

[25] Geert Smet et al. "Managing Reaction Wheel Microvibration on a High Resolution EO Small Spacecraft". In: *ESMATS 2013*. 2013.

[26] H. Heimel. "Spacewheel Microvibration - Sources, Appearance, Countermeasures". In: *8th International ESA Conference onGuidance, Navigation and Control Systems*. 2011.

[27] J. Maly et al. "Hubble Space Telescope solar array damper". In: *Symposium on Smart Structures and Materials*. 1999.

[28] Chunchuan Liu et al. "Recent advances in micro-vibration isolation". In: *Mechanical Systems and Signal Processing* 56-57 (2015), pp. 55–80. DOI: 10.1016/j.ymssp.2014.10.007.

[29] L. Vaillon and C. Philippe. "Passive and active microvibration control for very high pointing accuracy space systems". In: *Smart Mater. Struct. 8* (1999).

[30] M. Algrain, D.Ehlers, and S.Hardt. "Autonomous smart sensor-electronics-actuator device for controlling periodic vibration in a structural system". In: *Proceedings of the Smart Structures and Integrated Systems* (1997).

[31] Larry Davis et al. "Adaptive neural control for space structure vibration suppression". In: *Smart Materials and Structures* 8.6 (1999), pp. 753–766. DOI: 10.1088/0964-1726/8/6/305.

[32] Chaoxin Wang et al. "Investigation on active vibration isolation of a Stewart platform with piezoelectric actuators". In: *Journal of Sound and Vibration* 383 (2016), pp. 1–19. DOI: 10.1016/j.jsv.2016.07.021.

[33] D. Kamesh, R. Pandiyan, and Ashitava Ghosal. "Modeling, design and analysis of low frequency platform for attenuating micro-vibration in spacecraft". In: *Journal of Sound and Vibration* 329.17 (2010), pp. 3431–3450. DOI: 10.1016/j.jsv.2010.03.008.

[34] Richard G Cobb et al. “Vibration isolation and suppression system for precision payloads in space”. In: *Smart Materials and Structures* 8.6 (1999), pp. 798–812. DOI: 10.1088/0964-1726/8/6/309.

[35] Fabrice Boquet, Florence Malric-Smith, and Jean-Pascal Lejault. “Active and passive microvibration mitigation system for earth observation and space science missions”. In: *Advances in the Astronautical Sciences* (2011).

[36] Federico Secondi. “Robust active control for microvibration mitigation in high sta-bility space missions”. PhD thesis. Politecnico di Milano, 2013.

[37] Alexandre Falcoz et al. “Active VibrationControl and Isolation: The LPV Way”. In: *ESA-CNES-DLR Workshop "Linear Parameter Varying Control: A Framework for Adaptable Space Systems"* (2014).

[38] Thierry Blais and Frederic Di Gesu. “Fine steering mechanism for new generation optical communication terminals”. In: *Proceedings of the 8th European Space Mechanisms and Tribology Symposium* (1999).

[39] Qinkqun Zhou. “Design Analysis of Fine Steering Mirror”. In: *Sensors et actuators* (2009).

[40] T. Shimizu et al. “Image Stabilization System for Hinode (Solar-B) Solar Optical Telescope”. In: *Solar Physics* 249.2 (2007), pp. 221–232. DOI: 10.1007/s11207-007-9053-z.

[41] Stefan Kuiper, Will Crowcombe, and Jet Human. “High-bandwidth and compact fine steering mirror development for laser communications”. In: *Proc. ESMATS 2017, Univ. of Hertfordshire, Hatfield, U.K., 2022 September 2017* (2017).

[42] Florence Yver-Leduc et al. “Reaching the quantum noise limit in a high-sensitivity cold-atom inertial sensor”. In: *Journal of Optics B: Quantum and Semiclassical Optics* 5.2 (2003), S136–S142. DOI: 10.1088/1464-4266/5/2/371.

[43] P. Cheinet et al. “Measurement of the sensitivity function in time-domain atomic interferometer”. In: *IEEE Trans. on Instrum. Measur. 2005*. IEEE, 2005.

[44] R. Geiger et al. “Detecting inertial effects with airborne matter-wave interferometry”. In: *Nature Communications* 2.1 (2011). DOI: 10.1038/ncomms1479.

[45] B. Fang et al. “Metrology with Atom Interferometry: Inertial Sensors from Laboratory to Field Applications”. In: *Journal of Physics: Conference Series 723* (2016).

[46] Hyosang Yoon. "Pointing System Performance Analysis for optical inter-satellite communication on cubesats". PhD thesis. Massachusetts Institue of Technology, 2017.

[47] K. Araki and T. Aruga. "Space optical communication technologies - an overview". In: *Rev. Laser Eng. 24* (1996).

[48] Morio Toyoshima et al. "Optimum divergence angle of a Gaussian beam wave in the presence of random jitter in free-space laser communication systems". In: *Journal of the Optical Society of America A* 19.3 (2002), p. 567. DOI: 10.1364/josaa.19.000567.

[49] L. Soula. *Methodology for analysis of structure-borne micro-vibrations (METAMIC) State of the art of structural micro-vibration analysis and test*. Tech. rep. ESA Contract 4000101886/10/NL/RA, 2011.

[50] Maurus Kaufmann et al. "High-speed magnetically levitated reaction wheels for small satellites". In: *2016 International Symposium on Power Electronics, Electrical Drives, Automation and Motion (SPEEDAM)*. IEEE, 2016. DOI: 10.1109/speedam.2016.7525889.

[51] B. Bialke. "Microvibration disturbance fundamentals for rotating mechanisms". In: *34th Annual Guidance and Control Conference, American Astronautical Society* (2011).

[52] Howard D. Curtis. *Orbital Mechanics for Engineering Students*. Elsevier, 2014, pp. 1–57. DOI: 10.1016/b978-0-08-097747-8.00001-3.

[53] Renny Fields et al. "NFIRE-to-TerraSAR-X laser communication results: satellite pointing, disturbances, and other attributes consistent with successful performance". In: *Sensors and Systems for Space Applications III*. Ed. by Joseph L. Cox and Pejmun Motaghedi. SPIE, 2009. DOI: 10.1117/12.820393.

[54] H.Luebberstedt et al. *Electra-Full Electric Propulsion Satellite Platform for GEO Missions$_{f}$inal$_{B}$*. Tech. rep. OHB System, 2018.

[55] James R. Wertz and Wiley J. Larson. *Space Mission Analysis and Design*. Ed. by Wiley. Microcosm Press, 1999.

[56] J. Martin et al. "Eurostar 3000 AOCS Design". In: *Proceedings 4th ESA International Conference on Spacecraft Guidance, Navigation and Control Systems* (1999).

[57] Jonas Marie et al. "In-orbit experience of the Gaia and LISA Pathfinder cold gas micro-propulsion systems". In: *2018 SpaceOps Conference*. American Institute of Aeronautics and Astronautics, 2018. DOI: 10.2514/6.2018-2716.

[58] Ho-Nien Shou. "Microsatellite Attitude Determination and Control SubsystemDesign and Implementation: Software-in-the-Loop Approach". In: *Mathematical Problems in Engineering* (2014).

[59] R. Engel and F. Fleig. *Satellite Structure Model Microvibration Report*. Tech. rep. OHB System, 2012.

[60] A. Grillenbeck, G. Deutsch, and B. Pouilloux. "Micro-vibration measurements on thermally loaded multi-layer insulation samples". In: *1st CEAS European Air and Space Conference* (2007).